

A consistent mixed-dimensional coupling approach for 1D Cosserat beams and 2D solid surfaces

Ivo Steinbrecher · Nora Hagemeyer · Christoph Meier · Alexander Popp

Received: date / Accepted: date

Abstract The present article proposes a novel computational method for coupling 1D fibers with the 2D surface of a 3D solid. The fibers are modeled as 1D Cosserat continua (beams) with six local degrees of freedom, three positional and three rotational ones. A kinematically consistent 1D-2D coupling scheme for this problem type is proposed considering the positional and rotational degrees of freedom along the beams. The positional degrees of freedom are coupled by enforcing a constant normal distance between a point on the beam centerline and a corresponding point on the solid surface. This strategy requires a consistent description of the solid surface normal vector field to guarantee fundamental mechanical properties such as conservation of angular momentum. Coupling of the rotational degrees of freedom of the beams and a suitable rotation tensor representative for the local orientation within a Boltzmann continuum has been considered in a previous contribution. In the present work, this coupling approach will be extended by constructing rotation tensors that are representative for local surface orientations. Several numerical examples demonstrate the consistency, robustness and accuracy of the proposed method. To showcase its applicability to multi-physics systems of practical relevance, the fluid-structure interaction example of a vascular stent is presented.

Keywords Beam-to-surface coupling · 1D-2D position and rotation coupling · Mixed-dimensional coupling · Finite

element method · Geometrically exact beam theory · Mortar methods

1 Introduction

Compound structures consisting of one-dimensional (1D) beam-like structures, i.e., structures with one spatial dimension being much larger than the other two, tied to three-dimensional (3D) solid continua can be found in a variety of different fields. From a geometrical point of view, the problem considered in the present work consists of 1D beams coupled to the two-dimensional (2D) surface of a 3D continuum (solid). This will be denoted as beam-to-solid surface (BTSS) coupling problem throughout this contribution. Applications for this class of problems can be found in, e.g., civil engineering, where steel girders are used to support concrete slabs, or in mechanical engineering, where lightweight structures are realized by stabilizing thin shells with struts. Leaving the realm of classical engineering applications, BTSS coupling approaches can also be used to model biomechanical systems, for example to capture the interaction between stent and graft (encasing fabric) as used for endovascular aneurysm repair. Numerical simulation of such applications is of high importance during the development and design phase to accurately predict and control the desired system behavior.

The present modeling approach for the BTSS coupling problem employs accurate and efficient 1D models for the beam-like structures based on geometrically exact beam theory [5, 9, 12, 20, 35, 47, 48, 51–53]. The beams are represented by 1D curves in 3D space, i.e., the beam centerline that connects the centroids of the beam cross-sections. Each point along the beam centerline has six degrees of freedom (three positional and three rotational ones), i.e., the beam model can be identified as a 1D Cosserat continuum. The solid

I. Steinbrecher, N. Hagemeyer, A. Popp
Institute for Mathematics and Computer-Based Simulation,
University of the Bundeswehr Munich,
Werner-Heisenberg-Weg 39, D-85577 Neubiberg, Germany
E-mail: ivo.steinbrecher@unibw.de

C. Meier
Institute for Computational Mechanics,
Technical University of Munich,
Boltzmannstrasse 15, D-85748 Garching b. München, Germany

body is modeled as a classical 3D Boltzmann continuum. The 1D beams are coupled to the 2D surfaces of the 3D continua, thus resulting in a mixed-dimensional 1D-2D coupling problem. The resulting BTSS coupling problem has two desirable features, cf. [55, 57]: (i) Both the solid and the beam can be modeled and discretized individually. Therefore, well-established discretization schemes for the solid and the beam can be used without modifications. (ii) Employing 1D beam models results in computationally efficient finite element discretizations, which reduces the number of unknowns required to represent the beam-like structures by several orders of magnitude as compared to a modeling approach based on 3D continuum theory. In the literature, mixed-dimensional coupling between structural beam theories and solid continua is often addressed to model fiber-reinforced materials, e.g., [10, 15, 18, 23, 38, 46]. However, in all of the aforementioned works, the coupling is an embedded 1D-3D coupling since the 1D fiber reinforcements are placed inside the solid domain and are directly coupled to the 3D solid volume. Furthermore, 1D string-like models with a limited representation of the relevant modes of deformation, i.e., only axial deformation, were used in these contributions to represent the 1D curves. Coupling approaches for full beam theories in 1D-3D beam-to-solid volume (BTSV) coupling problems have been developed more recently, e.g., in [14, 24, 55, 57]. Compared to the previously mentioned string models, beam theories contain additional deformation modes, i.e., bending, torsion and shear, which allows for a more realistic representation of the nonlinear force-displacement relations caused by the reinforcements. In [14] a collocation method is used to couple the beams to the solid. A mortar-type approach to couple the positional degrees of freedom of the beam centerline to the solid is presented in [55] and a mortar-type approach for *full* coupling, i.e., positional *and* rotational coupling, is presented in [57]. In [24] the coupling constraints of a BTSV problem are formulated on the surface of the beam and are subsequently projected onto the beam centerline considering a Taylor series expansion of the solid displacement field. Apart from the 1D-3D coupling problems discussed so far, a truly 1D-2D coupling is presented in [29]. However, the solid surfaces are assumed to be rigid in that contribution, which heavily limits the applicability to real life engineering problems.

In the present work, we propose the first truly mixed-dimensional 1D-2D mortar-type approach for BTSS coupling problems. This is an extension of the authors' previous contributions on positional beam-to-solid volume (BTSV-POS) and rotational beam-to-solid volume (BTSV-ROT) coupling problems [55, 57] to BTSS coupling problems. The transition from a 1D-3D to a 1D-2D mixed-dimensional coupling introduces two additional challenges: (i) The positional BTSS coupling (BTSS-POS) constraints between the beam and the solid surface depend on the surface normal vector.

In this work, the term *consistent* implies that no simplifications regarding the surface normal vector are introduced in the further derivation of the positional coupling constraints. A consistent treatment of the surface normal vector, especially in the discretized problem setting can become cumbersome. Therefore, different possible simplifications of the consistent positional coupling constraints (BTSS-POS-(·)) are presented. As a main scientific contribution of this work, it is demonstrated that in the general case of non-matching 1D-2D interfaces only a fully consistent handling of the surface normal vector within the coupling constraints allows to fulfill fundamental mechanical properties and to give accurate results. In particular, exact conservation of linear and angular momentum is shown for the resulting 1D-2D coupling scheme. To the authors' best knowledge, this is the first time that exact conservation of angular momentum is shown for a surface coupling scheme with non-vanishing surface normal distance. (ii) For rotational BTSS (BTSS-ROT) coupling a suitable solid orientation field is required on the solid surface. A detailed discussion on rotation tensors that are representative for the local orientation of a solid continuum is given in [57]. However, a direct application of these approaches to solid surfaces leads to undesirable effects, i.e., the solid surface orientation would depend on the deformations inside the solid volume. Therefore, the second main scientific contribution of this work is the construction of a suitable solid surface orientation field. In the remainder of this work, BTSS-FULL refers to positional *and* rotational BTSS coupling.

Within this contribution the solid surface is exclusively considered as boundary of a three-dimensional solid volume. For standard Lagrangian finite element interpolations of the solid, the solid surface normal field is non-continuous across element edges. To recover C^0 -continuity, a re-interpolation scheme for the surface normal vectors is employed, comparable to the evaluation of the surface normal field in surface-to-surface contact schemes, e.g., [41, 64].

Eventually, it is emphasized that a modeling approach based on mixed-dimensional coupling influences the nature of the underlying mechanical problem. In the context of embedded 1D-3D coupling this issue has been thoroughly discussed and analyzed for the cases of positional coupling [55] and rotational coupling [57]. One of the main consequences is that the analytical solution of the mixed-dimensional coupling problem exhibits a local singularity at the position of the beam centerline. In the embedded 1D-3D positional coupling case this can be interpreted as a generalization of the well-known Kelvin problem [40, 59], cf. Figure 1(a), i.e., a line load acting on an infinite solid. The same issue arises in the considered case of 1D-2D BTSS coupling, which corresponds to the Flamant problem of a line load acting on an infinite half space [39], cf. Figure 1(b). However, similar to the BTSV case this aspect does not impact the applicability

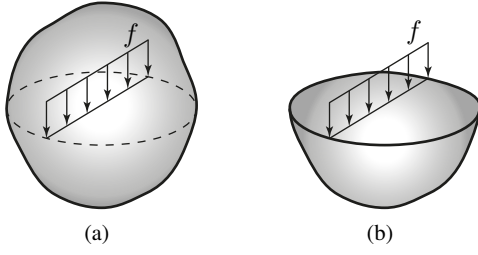


Fig. 1 (a) The Kelvin problem of an embedded line load acting on an infinite solid and (b) the Flamant problem of a line load acting on an infinite solid half space.

of the proposed BTSS coupling method for the envisioned range of practically relevant discretization resolutions, i.e., solid element sizes in the range of the beam cross-section diameter or above. As discussed in detail in [55, 57], the aforementioned singularity does not occur for this range of solid mesh sizes.

The remainder of this work is organized as follows: In Section 2, we state the governing equations for solid and beam formulations as well as for the BTSS-FULL method. In Section 3, a suitable procedure for constructing the solid surface triad is presented to couple the rotations of the solid surface to the beam cross-section orientations. The finite element discretization of the BTSS-FULL method is presented in Section 4. Furthermore, the construction of a C^0 -continuous surface normal field is elaborated. Finally, in Section 5, we present numerical examples to demonstrate the consistency of the presented BTSS-FULL method and the applicability to real-life engineering and biomedical problems. Detailed comparisons with full 3D continuum approaches, i.e., beam and solid are modeled as 3D continua and discretized by 3D solid finite elements, for the BTSS coupling problem are presented. Furthermore, the importance of coupling both positions *and* rotations for beam-to-solid surface coupling problems is shown.

2 Problem formulation

We consider a quasi-static 3D finite deformation BTSS-FULL coupling problem as shown in Figure 2. It is emphasized that the presented BTSS-FULL method is not restricted to quasi-static problems, but can directly be applied to time-dependent problems as well. A Cartesian frame $\mathbf{e}_1, \mathbf{e}_2$ and \mathbf{e}_3 serves as fixed frame of reference. The principle of virtual work (PVW) serves as basis for a subsequent finite element discretization and reads

$$\delta W^S + \delta W^B + \delta \Pi_\lambda = 0. \quad (1)$$

Here, δW^S is the total virtual work of the pure solid problem, δW^B is the total virtual work of the pure beam problem

and $\delta \Pi_\lambda$ is the virtual work due to coupling forces and moments. Contributions to the total virtual work of the pure solid and beam problem are independent of the coupling constraints, i.e., well-established modeling and discretization techniques can be used for the solid and the beam, cf. [55, 57].

2.1 Finite rotations

Before stating the governing equations for the solid, beam and BTSS-FULL coupling problem, a short recap on finite rotations is given here, as a consistent treatment of large rotations is required for the rotational coupling conditions BTSS-ROT. In geometrically exact beam theory, the term triad is commonly used to describe the set of three orthonormal vectors defining a beam cross-section orientation, i.e.,

$$\underline{\mathbf{A}} = [\underline{\mathbf{g}}_1, \underline{\mathbf{g}}_2, \underline{\mathbf{g}}_3] \in SO^3. \quad (2)$$

Here, SO^3 is the special orthogonal group and $\underline{\mathbf{g}}_i$ are the base vectors of the triad. The triad is equivalent to a rotation tensor, mapping the Cartesian basis vectors \mathbf{e}_i onto $\underline{\mathbf{g}}_i$. Among others, a triad can be parameterized by the rotation (pseudo-)vector $\underline{\boldsymbol{\psi}}$, i.e., $\underline{\mathbf{A}} = \underline{\mathbf{A}}(\underline{\boldsymbol{\psi}})$. The rotation vector describes a rotation by an angle $\psi = \|\underline{\boldsymbol{\psi}}\|$ around the rotation axis $\mathbf{e}_{\psi} = \underline{\boldsymbol{\psi}} / \|\underline{\boldsymbol{\psi}}\|$. The parametrization can be evaluated with the well-known Rodrigues formula [1]

$$\begin{aligned} \underline{\mathbf{A}}(\underline{\boldsymbol{\psi}}) &= \exp(\underline{\mathbf{S}}(\underline{\boldsymbol{\psi}})) \\ &= \underline{\mathbf{I}} + \sin \psi \underline{\mathbf{S}}(\mathbf{e}_{\psi}) + (1 - \cos \psi) \underline{\mathbf{S}}^2(\mathbf{e}_{\psi}), \end{aligned} \quad (3)$$

where $\exp(\cdot)$ is the exponential map and $\underline{\mathbf{S}}$ is a skew-symmetric tensor such that $\underline{\mathbf{S}}(\underline{\mathbf{a}})\underline{\mathbf{b}} = \underline{\mathbf{a}} \times \underline{\mathbf{b}} \forall \underline{\mathbf{a}}, \underline{\mathbf{b}} \in \mathbb{R}^3$. The calculation of the inverse of the Rodrigues formula is not straight forward. For simplicity, it is abbreviated by the expression $\underline{\boldsymbol{\psi}}(\underline{\mathbf{A}}) = \text{rv}(\underline{\mathbf{A}})$ in the following. In practice, Spurrier's algorithm [54] can be used for the extraction of the rotation vector. Let us consider two triads $\underline{\mathbf{A}}_1(\underline{\boldsymbol{\psi}}_1)$ and $\underline{\mathbf{A}}_2(\underline{\boldsymbol{\psi}}_2)$ with their respective rotation vectors $\underline{\boldsymbol{\psi}}_1$ and $\underline{\boldsymbol{\psi}}_2$. They are related to each other by the relative rotation $\underline{\mathbf{A}}_{21}(\underline{\boldsymbol{\psi}}_{21})$. The relative rotation is given by

$$\begin{aligned} \underline{\mathbf{A}}_2(\underline{\boldsymbol{\psi}}_2) &= \underline{\mathbf{A}}_{21}(\underline{\boldsymbol{\psi}}_{21})\underline{\mathbf{A}}_1(\underline{\boldsymbol{\psi}}_1) \\ &\Downarrow \\ \underline{\mathbf{A}}_{21}(\underline{\boldsymbol{\psi}}_{21}) &= \underline{\mathbf{A}}_2(\underline{\boldsymbol{\psi}}_2)\underline{\mathbf{A}}_1(\underline{\boldsymbol{\psi}}_1)^T, \end{aligned} \quad (4)$$

with the identity $\underline{\mathbf{A}}^T = \underline{\mathbf{A}}^{-1}$ for all elements of SO^3 . The relative rotation vector $\underline{\boldsymbol{\psi}}_{21} = \text{rv}(\underline{\mathbf{A}}_{21})$ describes the relative rotation between $\underline{\mathbf{A}}_1$ and $\underline{\mathbf{A}}_2$. Rotation vectors are non-additive, i.e., $\underline{\boldsymbol{\psi}}_{21} \neq \underline{\boldsymbol{\psi}}_2 - \underline{\boldsymbol{\psi}}_1$. For a more comprehensive treatment of this topic, the interested reader is referred to [4, 9, 20, 35, 48, 52]. In the following sections, both symbols $\underline{\mathbf{A}}$ and $\underline{\mathbf{R}}$ will be used to represent rotation tensors.

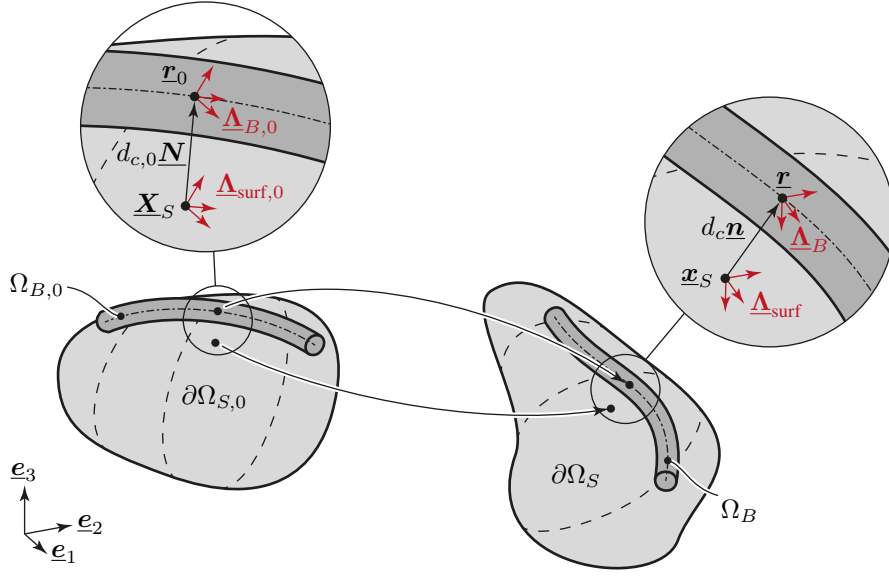


Fig. 2 Notation for the finite deformation BTSS-FULL coupling problem.

2.2 Solid formulation

The solid is modeled as a 3D Boltzmann continuum. The solid domain in the reference configuration is $\Omega_{S,0} \subset \mathbb{R}^3$ and $\partial\Omega_{S,0}$ is the boundary of the solid domain, i.e., the solid surface. Throughout this work, the subscript $(\cdot)_0$ indicates a quantity in the reference configuration. Accordingly, Ω_S and $\partial\Omega_S$ are the current solid domain and current solid surface, respectively. Furthermore, the current position $\mathbf{x}_S \in \mathbb{R}^3$ of a solid material point relates to the reference position $\mathbf{X}_S \in \mathbb{R}^3$ via the solid displacement field $\mathbf{u}_S \in \mathbb{R}^3$, i.e.,

$$\mathbf{x}_S(\mathbf{X}_S) = \mathbf{X}_S + \mathbf{u}_S(\mathbf{X}_S). \quad (5)$$

The virtual work contributions of the solid domain read

$$\begin{aligned} \delta W^S = & \int_{\Omega_{S,0}} \mathbf{S} : \delta \mathbf{E} dV_0 \\ & - \int_{\Omega_{S,0}} \hat{\mathbf{b}} \cdot \delta \mathbf{u}_S dV_0 - \int_{\Gamma_\sigma} \hat{\mathbf{t}} \cdot \delta \mathbf{u}_S dA_0. \end{aligned} \quad (6)$$

Here, δ denotes the (total) variation of a quantity, $\mathbf{S} \in \mathbb{R}^{3 \times 3}$ is the second Piola–Kirchhoff stress tensor, $\mathbf{E} = \frac{1}{2}(\mathbf{F}^T \mathbf{F} - \mathbf{I}) \in \mathbb{R}^{3 \times 3}$ is the work-conjugated Green–Lagrange strain tensor, $\hat{\mathbf{b}} \in \mathbb{R}^3$ is the body load vector and $\hat{\mathbf{t}} \in \mathbb{R}^3$ are surface tractions on the Neumann boundary $\Gamma_\sigma \subset \partial\Omega_{S,0}$. Furthermore, $\mathbf{F} \in \mathbb{R}^{3 \times 3}$ is the solid deformation gradient, which is defined according to

$$\mathbf{F} = \frac{\partial \mathbf{x}_S}{\partial \mathbf{X}_S}. \quad (7)$$

If e.g., a hyperelastic strain energy function $\Psi(\mathbf{E})$ exists, the constitutive relations between stresses and strains can be stated as $\mathbf{S} = \frac{\partial \Psi(\mathbf{E})}{\partial \mathbf{E}}$.

2.3 Geometrically exact beam theory

In this work the geometrically exact Simo–Reissner beam theory is used to describe the embedded beams as 1D Cosserat continua, e.g., [35, 47, 51, 52]. Each beam cross-section along the beam centerline is described by six degrees of freedom, three positional and three rotational ones, thus resulting in six deformation modes of the beam: axial tension, bending (2×), shear (2×) and torsion.

The complete beam kinematics can be defined by a centerline curve $\mathbf{r}(s) \in \mathbb{R}^3$, connecting the cross-section centroids, and a field of triads $\underline{\mathbf{A}}_B(s) = \underline{\mathbf{A}}_B(\psi_B(s))$ defining the orientation of the beam cross-sections. Here, $s \in [0, L] =: \Omega_{B,0}$ is the arc-length coordinate along the beam centerline in the reference configuration and L is the reference length of the beam. The triad $\underline{\mathbf{A}}_B$ is chosen such that the second and third basis vectors, \mathbf{g}_{B2} and \mathbf{g}_{B3} , span the beam cross-section, i.e., the first triad basis vector \mathbf{g}_{B1} is normal to the beam cross-section. A total hyperelastic stored-energy function of the Simo–Reissner beam can be stated as

$$\Pi_{\text{int},B} = \int_{\Omega_{B,0}} \tilde{\Pi}_{\text{int},B} ds, \quad (8)$$

with

$$\tilde{\Pi}_{\text{int},B} = \frac{1}{2}(\mathbf{I}^T \mathbf{C}_F \mathbf{I} + \mathbf{\Omega}^T \mathbf{C}_M \mathbf{\Omega}). \quad (9)$$

Here, $\mathbf{I} \in \mathbb{R}^3$ is a material deformation measure representing axial tension and shear, $\mathbf{\Omega} \in \mathbb{R}^3$ is a material deformation measure representing torsion and bending, and $\mathbf{C}_F \in \mathbb{R}^{3 \times 3}$ and $\mathbf{C}_M \in \mathbb{R}^{3 \times 3}$ are cross-section constitutive matrices. The material force stress resultants $\mathbf{F} = \partial \tilde{\Pi}_{\text{int},B} / \partial \mathbf{I}$ and moment stress resultants $\mathbf{M} = \partial \tilde{\Pi}_{\text{int},B} / \partial \mathbf{\Omega}$ can be derived

from the hyperelastic stored-energy function. Finally, the beam contributions to the weak form are given by

$$\delta W^B = \delta \Pi_{\text{int},B} + \delta W_{\text{ext}}^B, \quad (10)$$

where δW_{ext}^B is the virtual work of external forces and moments acting on the beam. For a more comprehensive presentation of the weak form of the geometrically exact Simo–Reissner beam theory, the interested reader is referred to [35].

2.4 Beam-to-solid surface coupling (BTSS-FULL)

The BTSS-FULL method proposed in this work couples all six cross-section degrees of freedom of the beam to the solid surface. This is realized by coupling the positions of the beam centerline as well as the orientation of the beam cross-section to the solid surface. One advantage of a 1D-2D coupling approach solely enforced at the beam centerline is the decoupling of the positional and rotational coupling conditions, i.e., both of them can be formulated independently. For embedded 1D geometrically exact beams in 3D solid volumes such an approach has recently been presented in [57]. The same general strategy is followed here for BTSS coupling problems, where we define two sets of coupling constraints, the positional coupling constraints (BTSS-POS) and the rotational coupling constraints (BTSS-ROT). With this split, the total BTSS-FULL coupling contribution to the weak form reads,

$$\delta \Pi_\lambda = \delta \Pi_{\lambda_r} + \delta \Pi_{\lambda_\theta}, \quad (11)$$

where $\delta \Pi_{\lambda_r}$ and $\delta \Pi_{\lambda_\theta}$ are the virtual work contributions from the positional and rotational coupling conditions, respectively.

2.4.1 Closest point projection

In the considered BTSS-FULL coupling problem, cf. Figure 2, no requirements on the initial beam position relative to the solid surface exist. This is illustrated in Figure 3. Obviously, the coupling scheme has to be applicable to cases where the beam centerline curve lies on the solid surface, cf. Figure 3(a), and cases where the beam centerline is offset by the cross-section radius in surface normal direction, cf. Figure 3(b). However, also general cases, where no strict requirements on the reference placement of the beam centerline relative to the solid surface are made, are considered in the presented coupling schemes, cf. Figure 3(c). The only requirement considered in this work is a unique closest point projection of each beam centerline point onto the solid surface. For the envisioned application cases, it can be assumed that a unique solution of the closest point projection exists in the vicinity of each beam centerline point \mathbf{r}_0 , cf. [28]. In order to formulate the closest point projection, the solid

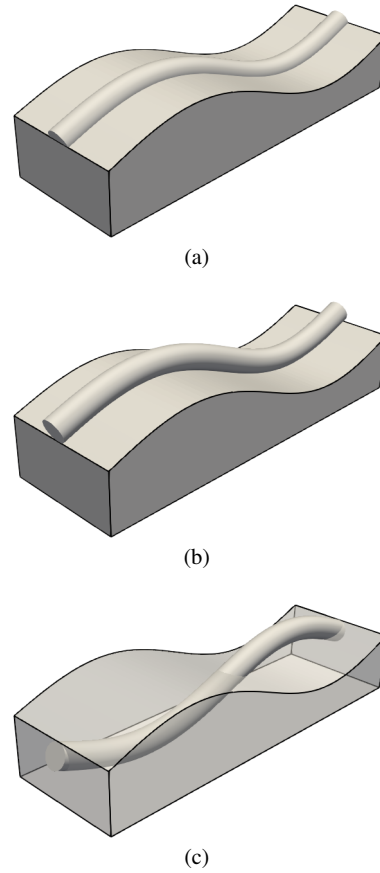


Fig. 3 Illustration of possible BTSS coupling problems – (a) a curved beam on a matching curved solid surface, (b) a curved beam centerline offset by the cross-section radius in surface normal direction and (c) a general non-matching case.

surface is parameterized with the two surface parameter coordinates $\xi^S \in \mathbb{R}$ and $\eta^S \in \mathbb{R}$. In the reference configuration each point $\mathbf{r}_0(s)$ on the beam centerline is assigned to a corresponding closest point $\underline{\mathbf{X}}_S(\xi_c^S, \eta_c^S)$ on the solid surface, where $\xi_c^S = \xi_c^S(s)$ and $\eta_c^S = \eta_c^S(s)$ are the surface parameter coordinates of the closest point. The closest point can be found by formulating a unilateral minimal distance problem in the reference configuration:

$$d_{c,0}(s) := \min_{\xi^S, \eta^S} d(s, \xi^S, \eta^S) = d(s, \xi_c^S, \eta_c^S) \quad (12)$$

with

$$d(s, \xi^S, \eta^S) = \|\mathbf{r}_0(s) - \underline{\mathbf{X}}_S(\xi^S, \eta^S)\|. \quad (13)$$

The two orthogonality conditions obtained from the minimal distance problem (12) read

$$\begin{aligned} \underline{\mathbf{X}}_{S,\xi^S}(\xi^S, \eta^S)^T (\mathbf{r}_0(s) - \underline{\mathbf{X}}_S(\xi^S, \eta^S)) &= 0, \\ \underline{\mathbf{X}}_{S,\eta^S}(\xi^S, \eta^S)^T (\mathbf{r}_0(s) - \underline{\mathbf{X}}_S(\xi^S, \eta^S)) &= 0. \end{aligned} \quad (14)$$

For a given beam coordinate s , these conditions can be solved for the unknown surface coordinates ξ^S and η^S .

The non-trivial solution of (14) requires the surface directors $\underline{\mathbf{X}}_{S,\xi^S} = \partial \underline{\mathbf{X}}_S / \partial \xi^S$ and $\underline{\mathbf{X}}_{S,\eta^S} = \partial \underline{\mathbf{X}}_S / \partial \eta^S$ to be orthogonal to the relative vector between the surface point and the beam centerline point, i.e., this relative vector is parallel to the outward pointing surface normal vector $\underline{\mathbf{N}} \in \mathbb{R}^3$,

$$\underline{\mathbf{r}}_0(s) - \underline{\mathbf{X}}_S(\xi_c^S, \eta_c^S) = d_{c,0}(s) \underline{\mathbf{N}}(\xi_c^S, \eta_c^S) \quad (15)$$

with

$$\underline{\mathbf{N}}(\xi^S, \eta^S) = \frac{\underline{\mathbf{X}}_{S,\xi^S}(\xi^S, \eta^S) \times \underline{\mathbf{X}}_{S,\eta^S}(\xi^S, \eta^S)}{\|\underline{\mathbf{X}}_{S,\xi^S}(\xi^S, \eta^S) \times \underline{\mathbf{X}}_{S,\eta^S}(\xi^S, \eta^S)\|}. \quad (16)$$

2.5 Positional beam-to-solid surface coupling (BTSS-POS)

In this section, three different variants of the BTSS-POS coupling constraints are presented. They will be compared with each other in more detail in Section 5. The first presented variant is consistent with the kinematic relations between beam centerline and solid surface. The resulting coupling terms contain the surface normal vector, i.e., the coupling terms become non-linear. Furthermore, the second derivative of the surface normal vector is required for a consistent linearization of the problem in tangent-based nonlinear solution schemes (such as the Newton–Raphson algorithm). To avoid this computationally expensive linearization, two additional variants to formulate the positional coupling constraints, commonly used in classical surface-to-surface mesh tying problems [43], will be investigated. Both of them do not require an evaluation of the current surface normal vector or its derivatives, and the resulting coupling operators only depend on the reference configuration, i.e., they are constant. The different coupling variants are visualized in Figure 4.

2.5.1 Consistent positional coupling (BTSS-POS-CONS)

The BTSS-POS coupling constraints are exclusively formulated along the beam centerline and couple the beam and solid material points associated by (15) to each other. For the considered consistent variant, the surface normal distance d_c at each beam centerline point shall be constant over the simulation (pseudo-)time, i.e., $d_c \equiv d_{c,0}$. Therefore, the coupling equations in the current configuration can be formulated as

$$\underline{\mathbf{r}}(s) - \underline{\mathbf{x}}_S(\xi_c^S, \eta_c^S) - d_{c,0}(s) \underline{\mathbf{n}}(\xi_c^S, \eta_c^S) = \underline{\mathbf{0}} \quad \text{on } \Gamma_c. \quad (17)$$

The current normal vector is defined in analogy to the reference normal vector (4), i.e.,

$$\underline{\mathbf{n}}(\xi_c^S, \eta_c^S) = \frac{\underline{\mathbf{x}}_{S,\xi^S}(\xi_c^S, \eta_c^S) \times \underline{\mathbf{x}}_{S,\eta^S}(\xi_c^S, \eta_c^S)}{\|\underline{\mathbf{x}}_{S,\xi^S}(\xi_c^S, \eta_c^S) \times \underline{\mathbf{x}}_{S,\eta^S}(\xi_c^S, \eta_c^S)\|}, \quad (18)$$

with the current surface directors $\underline{\mathbf{x}}_{S,\xi^S} = \partial \underline{\mathbf{x}}_S / \partial \xi^S$ and $\underline{\mathbf{x}}_{S,\eta^S} = \partial \underline{\mathbf{x}}_S / \partial \eta^S$. The constraints (17) are enforced along

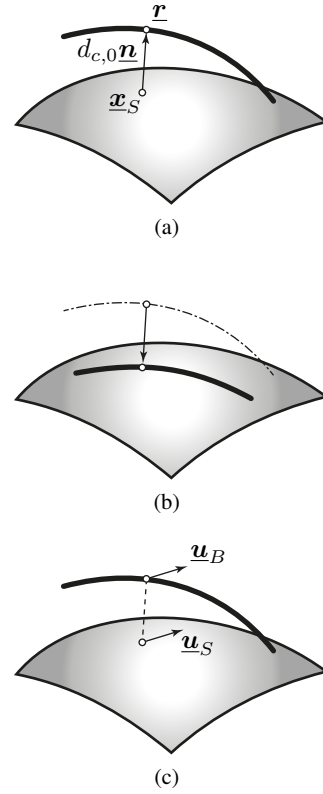


Fig. 4 Illustration of the different positional beam-to-solid surface (BTSS-POS) coupling variants. (a) Consistent positional coupling (BTSS-POS-CONS) via the surface normal vector, (b) forced reference configuration coupling (BTSS-POS-REF) by forcing beam centerline points to lie on the solid surface and (c) displacement coupling (BTSS-POS-DISP), where the displacement of beam centerline and solid surface are coupled. The surface-to-surface equivalents of the BTSS-POS-REF and BTSS-POS-DISP variants are commonly used in classical surface-to-surface mesh tying problems [43].

the one-dimensional coupling domain $\Gamma_c \subseteq \Omega_{B,0}$ between the beam centerline and the solid surface, i.e., the part of the beam that is coupled to the solid surface. In the following considerations, the explicit dependency on the beam and solid parameter coordinates will mostly be omitted for improved readability.

In the remainder of this work, the positional coupling constraints (17) will be referred to as the *consistent* (BTSS-POS-CONS) surface coupling variant. The name refers to the fact that the coupling definition is consistent with the kinematic relations between solid surface and beam centerline, cf. Figure 4(a). Furthermore, it will be shown that this variant leads to vanishing constraint forces in the (undeformed) reference configuration and exact conservation of linear and angular momentum in the discretized coupled system, cf. Section 4.5.3.

The Lagrange multiplier method is used to weakly enforce the coupling constraints (17). Therefore, a Lagrange multiplier vector field $\underline{\lambda}_r(s) \in \mathbb{R}^3$, defined along the beam

centerline, is introduced. The total Lagrange multiplier potential reads:

$$\Pi_{\lambda_r} = \int_{\Gamma_c} \boldsymbol{\lambda}_r^T (\mathbf{r} - \mathbf{x}_S - d_{c,0} \mathbf{n}) \, ds. \quad (19)$$

Variation of the Lagrange multiplier potential leads to the constraint contribution to the weak form,

$$\begin{aligned} \delta \Pi_{\lambda_r} = & \underbrace{\int_{\Gamma_c} \delta \boldsymbol{\lambda}_r^T (\mathbf{r} - \mathbf{x}_S - d_{c,0} \mathbf{n}) \, ds}_{\delta W_{\lambda_r}} \\ & + \underbrace{\int_{\Gamma_c} \boldsymbol{\lambda}_r^T (\delta \mathbf{r} - \delta \mathbf{x}_S - d_{c,0} \delta \mathbf{n}) \, ds}_{-\delta W_{C_r}}. \end{aligned} \quad (20)$$

Therein, δW_{λ_r} and δW_{C_r} are the variational form of the coupling constraints and the virtual work of the Lagrange multiplier field $\boldsymbol{\lambda}_r$, respectively. It is well-known from geometrically exact beam theory that the variation of the centerline position $\delta \mathbf{r}$ is work-conjugated with the point-wise forces acting on the beam centerline, i.e., $\boldsymbol{\lambda}_r \, ds$. Therefore, the Lagrange multiplier field $\boldsymbol{\lambda}_r$ can be directly interpreted as the coupling line load acting on the beam centerline. On the solid side, the variation of the solid displacement $\delta \mathbf{x}_S$ is work conjugated with the point-wise force $-\boldsymbol{\lambda}_r \, ds$ acting on the solid, i.e., the (negative) Lagrange multiplier field also acts as a line load on the solid. Additionally, the term $d_{c,0} \boldsymbol{\lambda}_r^T \delta \mathbf{n} \, ds$ arises, which represents a point-wise moment contribution of the coupling line load on the solid. If the beam centerline lies exactly on the beam surface, i.e., $d_{c,0} \equiv 0$, the BTSS-POS-CONS method (in the space continuous form) is equivalent to the BTV-POS method, cf. [55]. The drawback of the BTSS-POS-CONS variant is that for general scenarios the weak form contains the surface normal vector variation, thus requiring the second derivatives of the surface normal vector for a consistent linearization of $\delta \mathbf{n}$ as required for tangent-based nonlinear solution schemes. Furthermore, the positional coupling operators become non-linear due to this contribution, i.e., they depend on the current configuration.

2.5.2 Forced reference configuration coupling (BTSS-POS-REF)

The considered 1D-2D line-to-surface coupling constraints are very similar to the ones in classical 2D-2D surface-to-surface coupling problems, cf. [13, 37, 43]. In such problems, the space continuous interfaces are usually matching, i.e., the normal distance vanishes. Even if the surfaces do not match exactly, e.g., due to incompatible CAD files, the influence of the surface normal vector can usually be neglected since it is in the range of the discretization error. Therefore, the coupling constraints (17) can be simplified to

$$\mathbf{r} - \mathbf{x}_S = \mathbf{0} \quad \text{on} \quad \Gamma_c. \quad (21)$$

This type of positional coupling constraint will be referred to as the *forced reference configuration* surface coupling (BTSS-POS-REF). The Lagrange multiplier coupling contributions to the global weak form read

$$\delta W_{\lambda_r}^{\text{REF}} = \int_{\Gamma_c} \delta \boldsymbol{\lambda}_r^T (\mathbf{r} - \mathbf{x}_S) \, ds \quad (22)$$

$$-\delta W_{C_r}^{\text{REF}} = \int_{\Gamma_c} \boldsymbol{\lambda}_r^T (\delta \mathbf{r} - \delta \mathbf{x}_S) \, ds. \quad (23)$$

In this case, the surface normal vector is not contained in the resulting coupling equations, thus simplifying the numerical evaluation of the coupling terms. However, the coupling constraints (21) in the reference configuration are only fulfilled if the beam centerline lies exactly on the solid surface, i.e., $d_{c,0} \equiv 0$. If the beam centerline is not a subset of the solid surface, the coupling constraints (21) will lead to non-vanishing virtual work contributions in the reference configuration, i.e., initial stresses and deformations in the unloaded coupled system. In other words, the BTSS-POS-REF coupling conditions force the beam centerline to exactly lie on the solid surface, which is illustrated in Figure 4(b).

2.5.3 Displacement coupling (BTSS-POS-DISP)

Another alternative coupling approach in surface-to-surface mesh tying is to directly couple the displacements instead of the positions in (21). This variant will be referred to as the *displacement* surface coupling (BTSS-POS-DISP). The BTSS-POS-DISP coupling constraints read,

$$\mathbf{u}_B - \mathbf{u}_S = \mathbf{0} \quad \text{on} \quad \Gamma_c, \quad (24)$$

with the beam centerline displacement $\mathbf{u}_B = \mathbf{r} - \mathbf{r}_0$. The Lagrange multiplier coupling contributions to the global weak form are

$$\delta W_{\lambda_r}^{\text{DISP}} = \int_{\Gamma_c} \delta \boldsymbol{\lambda}_r^T (\mathbf{u}_B - \mathbf{u}_S) \, ds \quad (25)$$

$$-\delta W_{C_r}^{\text{DISP}} = \int_{\Gamma_c} \boldsymbol{\lambda}_r^T (\delta \mathbf{u}_B - \delta \mathbf{u}_S) \, ds. \quad (26)$$

As is the case for the BTSS-POS-REF variant, the normal vector does not appear in the coupling constraints. In this case, the coupling conditions are always fulfilled in the reference configuration no matter if the initial geometries of beam centerline and solid surface are matching or not. In [43] it is demonstrated that displacement coupling (24) can lead to a coupling formulation that does not conserve angular momentum. This can be shown by inserting a constant virtual rotation $\delta \boldsymbol{\phi}$, i.e., $\delta \mathbf{u}_B = \delta \boldsymbol{\phi} \times \mathbf{r}$ and $\delta \mathbf{u}_S = \delta \boldsymbol{\phi} \times \mathbf{x}_S$, into (26). To guarantee conservation of angular momentum the resulting virtual work has to vanish, cf. [43]. This gives the condition for conservation of angular momentum

$$\int_{\Gamma_c} (\delta \boldsymbol{\phi} \times (\mathbf{r} - \mathbf{x}_S))^T \boldsymbol{\lambda}_r \, ds = 0. \quad (27)$$

This condition is only fulfilled if $\mathbf{r} = \mathbf{x}_S$, i.e., for matching interfaces. For general configurations of the beam and the solid, i.e., when the beam centerline is offset in surface normal direction, conservation of angular momentum is violated by the BTSS-POS-DISP variant. This can also be interpreted from a mechanical point of view: displacement coupling of two points (a point on the beam centerline and the corresponding projection point on the solid surface) that do not coincide in the reference configuration, cf. Figure 4(c), leads to a non-physical coupling moment, which violates the conservation of angular momentum.

2.6 Rotational beam-to-solid surface coupling (BTSS-ROT)

Rotational beam-to-solid volume (BTSV-ROT) coupling between an embedded geometrically exact beam with a Boltzmann continuum has recently been presented and thoroughly discussed [57]. There, it has been shown that constraining the relative rotation (pseudo-)vector $\underline{\psi}_{SB}$ between the current beam triad $\underline{\mathbf{A}}_B$ and a suitable solid triad $\underline{\mathbf{A}}_S$ along the beam centerline leads to an objective coupling scheme. This approach is in accordance to general cross-section interaction laws within the geometrically exact beam theory, cf. [32]. This type of rotational coupling scheme can also be adopted for the presented case of BTSS coupling problems. The general approach is the same as in [57], but instead of a solid volume triad field, a suitable solid *surface* triad field has to be constructed. This construction procedure will be presented in Section 3. The rotational coupling constants constrain the relative rotation vector between the beam triad and a corresponding solid surface triad $\underline{\mathbf{A}}_{\text{surf}}$, i.e.,

$$\underline{\psi}_{SB} = \mathbf{0} \quad \text{on} \quad \Gamma_c, \quad (28)$$

with

$$\underline{\psi}_{SB} = \text{rv}(\underline{\mathbf{A}}_{\text{surf}} \underline{\mathbf{A}}_B^T). \quad (29)$$

The Lagrange multiplier method is used to weakly enforce the rotational coupling constraints (28). The corresponding weak form has been derived and thoroughly discussed in [57, Section 4.3.2] and will not be stated here.

3 Surface triad field

The rotational coupling conditions (28) constrain the relative rotation vector $\underline{\psi}_{SB}$ between the beam cross-section triad $\underline{\mathbf{A}}_B$ and a corresponding solid surface triad $\underline{\mathbf{A}}_{\text{surf}}$. The solid is modeled as a Boltzmann continuum, i.e., it does not have any rotational degrees of freedom. Therefore, a suitable solid surface triad field has to be constructed as a function of the solid deformation field. The construction of solid triad fields has very recently been thoroughly discussed

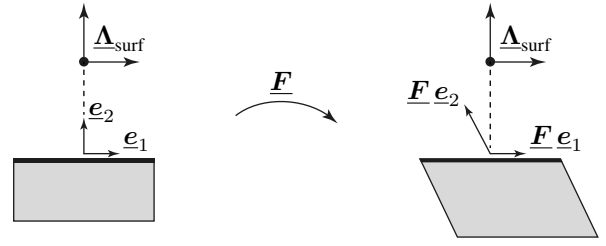


Fig. 5 Illustration of the influence of out of plane solid deformations on the solid deformation gradient at the solid surface.

and analyzed in [57]. There, two important attributes of the constructed triad field are identified: (i) The solid triad field has to be invariant with respect to an arbitrary rigid body rotation, such that the rotational coupling constraints (28) lead to an objective discrete coupling formulation. (ii) The resulting solid triad field should not constrain shear deformations in the beam cross-section plane, as this can result in spurious stiffening / locking effects of the coupled system. It has been shown in [57] that the rotation tensor obtained via a polar decomposition of the (in-plane projection of the) solid deformation gradient fulfills both aforementioned properties and represents the solid material directors in an L_2 -optimal manner. Furthermore, a slightly modified construction of the solid triad was presented that fixes an averaged solid material director to the solid triad. In practice, this modified variant gives very similar results compared to the solid triad obtained from the polar decomposition and also fulfills both aforementioned properties. Moreover, this variant avoids the computationally expensive evaluation of the polar decomposition (and its second derivatives) at Gauss-point level. In this section, we present a novel extension of this solid triad definition to end up with a suitable solid triad for BTSS coupling problems, that fulfills both aforementioned properties.

For the solid volume triads in [57] the (in-plane projection of the) solid deformation gradient $\underline{\mathbf{F}}$ was used. In theory, the solid volume triad definitions from [57] can also be applied to the considered BTSS problem, where the solid deformation gradient is evaluated at the solid surface. However, in this case the surface triad field would not only depend on the surface deformation, but also on the deformation inside the solid volume. This is illustrated in Figure 5, where the solid exhibits deformations inside the solid volume, while the surface geometry stays the same. The solid deformation gradient at the solid surface changes due to the deformation of material fibers inside the solid volume. However, from an intuitive physical point of view the *orientation* of the solid surface does not change. Therefore, we propose a different approach, where the resulting solid surface triad is constructed directly based on the surface kinematics, i.e., the two surface basis vectors and the surface normal vector.

The proposed construction of the surface triad is based on a material director $\underline{\mathbf{g}}$ lying on the solid surface, in com-

bination with the surface normal vector. The obvious and intuitive choice for this solid material director is the intersection between the beam cross-section plane and the solid surface tangent plane in the reference configuration, cf. Figure 6, which reads

$$\tilde{\mathbf{g}}_0 = \frac{\mathbf{N} \times \mathbf{g}_{B1,0}}{\|\mathbf{N} \times \mathbf{g}_{B1,0}\|}. \quad (30)$$

Theoretically, this definition of the solid material director can result in a singularity if the beam cross-section and the surface tangent plane are parallel to each other. However, since this would mean that the beam centerline is normal to the solid surface, this singularity will not be relevant for practical applications. The solid surface triad in the reference configuration can subsequently be constructed based on the solid material director and the solid surface normal vector, i.e.,

$$\tilde{\mathbf{A}}_{\text{surf},0} = [\tilde{\mathbf{g}}_0, \mathbf{N}, \tilde{\mathbf{g}}_0 \times \mathbf{N}]. \quad (31)$$

The solid material director in the current configuration $\tilde{\mathbf{g}}$ is calculated by applying the push-forward operator $\underline{\mathbf{F}}$ to the material director in the reference configuration, i.e., $\tilde{\mathbf{g}} = \underline{\mathbf{F}} \tilde{\mathbf{g}}_0 / \|\underline{\mathbf{F}} \tilde{\mathbf{g}}_0\|$. The previously mentioned dependency of the deformation gradient on deformations inside the solid volume does not affect this projection, as $\tilde{\mathbf{g}}_0$ lies within the solid surface, i.e., the projection only depends on the in-plane components of $\underline{\mathbf{F}}$. With the current solid material director, the surface triad in the current configuration can be constructed in analogy to (31), i.e.,

$$\tilde{\mathbf{A}}_{\text{surf}} = [\tilde{\mathbf{g}}, \mathbf{n}, \tilde{\mathbf{g}} \times \mathbf{n}]. \quad (32)$$

In a final step, the actual surface triad used for evaluation of the coupling terms has to be offset by a constant rotation, such that the rotational constraint equations (29) are fulfilled in the reference configuration. The final surface triad reads,

$$\mathbf{A}_{\text{surf}} = \tilde{\mathbf{A}}_{\text{surf}} \tilde{\mathbf{A}}_{\text{surf},0}^T \mathbf{A}_{B,0}. \quad (33)$$

With this definition, it is straight-forward to show that the surface triad in the reference configuration is equal to the beam reference triad, i.e., $\mathbf{A}_{\text{surf},0} = \mathbf{A}_{B,0}$ and therefore, the rotational coupling constraints are fulfilled in the reference configuration. It can also be shown that the surface triad definition (33) is invariant with respect to a superposed rigid body rotation, thus fulfilling requirement (i) stated above. Furthermore, since the surface triad is constructed based on a single material director $\tilde{\mathbf{g}}$ and the surface normal vector, a constraining of shear deformations on the solid surface can not occur. Therefore, the presented solid surface triad also fulfills requirement (ii).

Remark 3.1 To ensure a unique closest point projection in the spatially discretized problem, an averaged C^0 -continuous surface normal field is presented in Section 4.1. Due to the averaging procedure, the resulting averaged normal is not point-wise orthogonal to the solid surface, cf. Figure 7. With the definition of the surface triad (32), this would result in a non-orthonormal tensor $\mathbf{A}_{\text{surf}} \notin SO^3$. Therefore, the actual point-wise orthogonal normal vector on the surface, not the averaged normal vector, is used in the evaluation of the surface triad.

4 Spatial discretization

In this work, the spatial discretization is exclusively based on the finite element method. In the following, a subscript $(\cdot)_h$ refers to an interpolated field quantity. The solid domain is discretized with an isoparametric Bubnov–Galerkin finite element approach, i.e., position, displacement and virtual displacement field are discretized with the same shape functions. In the following derivation of the discretized coupling terms, only the discretized solid surface field is required, which is parameterized by the two surface parameter coordinates ξ^S and η^S . The spatial interpolation of the solid surface is given by

$$\underline{\mathbf{x}}_h^S = \sum_{k=1}^{n_I} N_k(\xi^S, \eta^S) \underline{\mathbf{x}}_k^S \quad (34)$$

$$\underline{\mathbf{u}}_h^S = \sum_{k=1}^{n_I} N_k(\xi^S, \eta^S) \underline{\mathbf{d}}_k^S \quad (35)$$

$$\delta \underline{\mathbf{u}}_h^S = \sum_{k=1}^{n_I} N_k(\xi^S, \eta^S) \delta \underline{\mathbf{d}}_k^S. \quad (36)$$

Here, n_I is the number of solid surface nodes and $N_k \in \mathbb{R}$ is the finite element shape function associated with the solid surface node k . Furthermore, $\underline{\mathbf{x}}_k^S \in \mathbb{R}^3$, $\underline{\mathbf{d}}_k^S \in \mathbb{R}^3$ and $\delta \underline{\mathbf{d}}_k^S \in \mathbb{R}^3$ are the reference position, displacement, and virtual displacement of node k , respectively. According to (5), the current position of a surface node evaluates to $\underline{\mathbf{x}}_k^S = \underline{\mathbf{X}}_k^S + \underline{\mathbf{d}}_k^S$. The solid discretization in the examples section is exclusively based on standard C^0 -continuous Lagrangian finite element interpolation. However, this is by no means a restriction of the presented BTSS-FULL coupling method, which can also be directly applied to C^1 -continuous (or higher) isogeometric solid elements based on NURBS.

The beam centerline interpolation considered in this work is exclusively based on third-order Hermitian polynomials, cf. [35, 61]. In this case, each node contains six centerline degrees of freedom, the nodal position $\mathbf{r}_l^B \in \mathbb{R}^3$ and the nodal centerline tangent $\mathbf{t}_l^B \in \mathbb{R}^3$ at the beam node l . This yields a C^1 -continuous beam centerline interpolation according to

$$\mathbf{r}_h = \sum_{l=1}^{n_B} H_l^r(\xi^B) \mathbf{r}_l^B + H_l^t(\xi^B) \mathbf{t}_l^B. \quad (37)$$

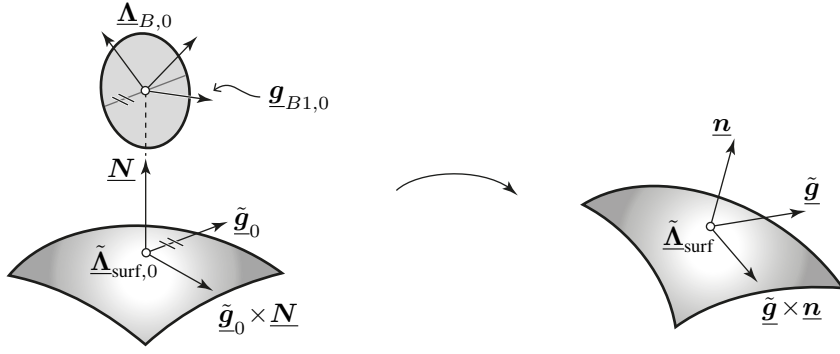


Fig. 6 Construction of the solid surface triad.

Here, n_B is the number of beam nodes and $H_l^r \in \mathbb{R}$ and $H_l^t \in \mathbb{R}$ denote the Hermite shape functions for the positional and tangential degrees of freedom of beam node l . Both shape functions have the scalar beam centerline parameter coordinate ξ^B as argument. At this point it is important to emphasize that the positional Hermite shape functions fulfill the partition of unity property, i.e., $\sum_{l=1}^{n_B} H_l^r \equiv 1$, cf. [33]. To improve readability the beam centerline interpolation (37) is rewritten in the following way

$$\underline{\mathbf{r}}_h = \sum_{l=1}^{n_B} \mathbf{H}_l(\xi^B) \mathbf{x}_l^B, \quad (38)$$

with

$$\mathbf{H}_l = [H_l^r \mathbf{I}^{3 \times 3} \quad H_l^t \mathbf{I}^{3 \times 3}] \in \mathbb{R}^{3 \times 6} \quad (39)$$

$$\mathbf{x}_l^B = \begin{bmatrix} \underline{\mathbf{r}}_l^B \\ \underline{\mathbf{t}}_l^B \end{bmatrix} \in \mathbb{R}^6. \quad (40)$$

Here, \mathbf{H}_l is the matrix with the node-wise assembled beam centerline shape functions and \mathbf{x}_l^B is the corresponding generalized nodal position vector. The discretized variation of the beam centerline position is given by

$$\delta \underline{\mathbf{r}}_h = \sum_{l=1}^{n_B} \mathbf{H}_l \delta \mathbf{d}_l^B, \quad \text{with} \quad \delta \mathbf{d}_l^B = \begin{bmatrix} \delta \underline{\mathbf{d}}_l^{B,r} \\ \delta \underline{\mathbf{d}}_l^{B,t} \end{bmatrix}. \quad (41)$$

Here $\delta \underline{\mathbf{d}}_l^{B,r} \in \mathbb{R}^3$ and $\delta \underline{\mathbf{d}}_l^{B,t} \in \mathbb{R}^3$ are the variations of the discrete nodal position and tangent, respectively. An objective and path-independent spatial interpolation of the beam cross-section rotations is a non-trivial task. The rotational interpolation only affects the BTSS-ROT coupling terms, which are entirely based on the BTSV-ROT method derived in [57], and will therefore not be stated here. For a more detailed discussion on this topic the interested reader is referred to [35, 57].

4.1 Evaluation of solid surface normal field

The closest point projection (12) of a point along the beam centerline to the solid surface requires a C^0 -continuous nor-

mal field onto guarantee a unique solution. If the solid discretization is based on isogeometric solid elements with higher order continuity, then the surface normal field can be directly calculated from the kinematic description of the discretized surface. The resulting surface normal field is at least C^0 -continuous and a unique closest point projection can be guaranteed. If a standard C^0 -continuous Lagrangian finite element interpolation is employed in the solid domain, the surface normal field obtained from the kinematic description of the discretized surface is not continuous. This can result in an undefined closest point projection. However, the beam-to-solid surface coupling scheme presented in this work is also applicable to such discretizations. This is achieved by constructing a C^0 -continuous normal field based on averaged nodal normal vectors, as is common in surface-to-surface problems, cf. [41, 64].

The main idea behind the construction of an averaged surface normal field is illustrated in Figure 7. An averaged nodal normal is defined at each surface node k as

$$\underline{\mathbf{n}}_{\text{AVG},k} = \frac{\sum_{e=1}^{n_{\text{adj},k}} \underline{\mathbf{n}}_k^{(e)}}{\left\| \sum_{e=1}^{n_{\text{adj},k}} \underline{\mathbf{n}}_k^{(e)} \right\|}, \quad (42)$$

where $\underline{\mathbf{n}}_k^{(e)}$ is the outward pointing surface normal vector of element e , evaluated at node k . Furthermore, $n_{\text{adj},k}$ represents the number of adjacent facets at node k . The final normal vector field is then defined via a FE interpolation, i.e.,

$$\underline{\mathbf{n}}_h(\xi^S, \eta^S) = \frac{\sum_{k=1}^{n_r} N_k(\xi^S, \eta^S) \underline{\mathbf{n}}_{\text{AVG},k}}{\left\| \sum_{k=1}^{n_r} N_k(\xi^S, \eta^S) \underline{\mathbf{n}}_{\text{AVG},k} \right\|}. \quad (43)$$

Such a surface normal field is guaranteed to be C^0 -continuous, i.e., it mimics a C^1 -continuous surface interpolation. However, one should admit that this procedure increases the computational effort required to evaluate the normal field and its derivatives. Additionally, the connectivity between element degrees of freedom is increased, as the normal on a solid face element depends on the degrees of freedom of the adjacent facets.

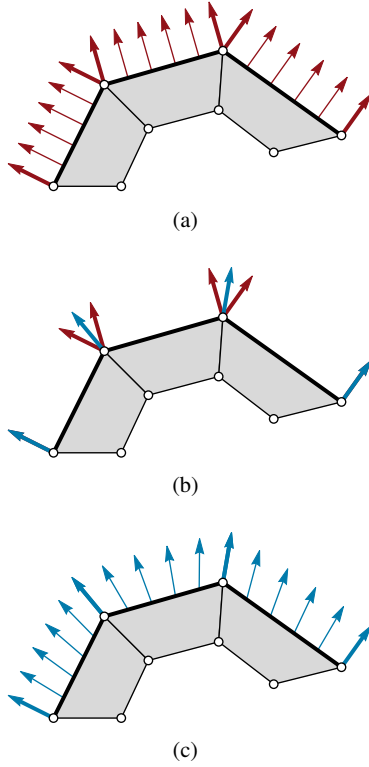


Fig. 7 Illustration of the constructed C^0 -continuous surface normal field, for an exemplary planar problem with three elements. (a) Discontinuous standard surface normal field based on the finite element surface kinematics, (b) averaged nodal normals and (c) C^0 -continuous interpolated averaged nodal normal field.

4.2 Uncoupled problem

Inserting the finite element approximations into the weak form of the equilibrium equations for the beam and solid problem and applying a standard Newton–Raphson procedure as nonlinear solution scheme yields the linearized global system of equations for the uncoupled problem,

$$\begin{bmatrix} \mathbf{K}_{ss}^S & \mathbf{0} & \mathbf{0} \\ \mathbf{0} & \mathbf{K}_{rr}^B & \mathbf{K}_{r\theta}^B \\ \mathbf{0} & \mathbf{K}_{\theta r}^B & \mathbf{K}_{\theta\theta}^B \end{bmatrix} \begin{bmatrix} \Delta \mathbf{d}^S \\ \Delta \mathbf{d}_r^B \\ \Delta \mathbf{d}_\theta^B \end{bmatrix} = \begin{bmatrix} -\mathbf{r}^S \\ -\mathbf{r}_r^B \\ -\mathbf{r}_\theta^B \end{bmatrix}. \quad (44)$$

Therein, \mathbf{K}_{ss}^S is the solid tangent stiffness matrix, $\Delta \mathbf{d}^S$ is the increment of the discrete solid degrees of freedom and \mathbf{r}^S is the residual force vector associated with the solid degrees of freedom. The beam degrees of freedom are split up into positional and rotational degrees of freedom, indicated by the subscripts r and θ , respectively. Accordingly, $\mathbf{K}_{(\cdot)(\cdot)}^B$ are the beam tangent stiffness matrices, $\Delta \mathbf{d}_{(\cdot)}^B$ are the increments of the beam degrees of freedom, and $\mathbf{r}_{(\cdot)}^B$ are the residual force vectors associated with the respective beam degrees of freedom.

The global solid displacement vector \mathbf{d}^S also contains degrees of freedom not related to the solid surface, i.e., the

number of total solid nodes n_S is (typically much) larger than the number of solid surface nodes n_Γ . However, a split of the solid degrees of freedom into surface and *inner* volume degrees of freedom is not introduced in what follows for improved readability.

4.3 Mortar-type coupling of beam-to-solid surface normal distance (BTSS-POS)

Similar to the BTSV-POS method introduced in [55], we employ a mortar-type coupling approach for all three positional coupling variants, i.e., the Lagrange multiplier field $\underline{\lambda}_r$ introduced in Section 2.4 is also interpolated with finite element shape functions, cf. [3, 41, 55, 63]. The discrete Lagrange multiplier field is defined along the discretized beam centerline. Its finite element interpolation reads

$$\underline{\lambda}_{r,h} = \sum_{j=1}^{n_\lambda} \Phi_{r,j}(\xi^B) \underline{\lambda}_{r,j}, \quad (45)$$

where n_λ is the total number of Lagrange multiplier nodes, $\Phi_{r,j}$ is the discrete Lagrange multiplier shape function of node j , and $\underline{\lambda}_{r,j} \in \mathbb{R}^3$ is the Lagrange multiplier at node j . Although defined along the beam centerline, there is no requirement for the Lagrange multiplier shape functions to match the shape functions used for interpolation of the beam centerline. Even the number of nodes can differ, i.e., $n_\lambda \neq n_B$.

The choice of Lagrange multiplier basis functions is important for the mathematical properties of the resulting discretized system. Generally speaking, the Lagrange multiplier interpolations must fulfill an inf-sup condition to guarantee stability of the mixed finite element method. We circumvent the inf-sup stability condition by employing a penalty regularized Lagrange multiplier approach. Detailed discussions regarding this topic can be found in [55] for the purely positional coupling BTSV-POS and in [57] for rotational coupling BTSV-ROT. The extensive studies and discussions in these works show that a linear interpolation of the Lagrange multipliers combined with a node-wise weighted penalty regularization generally leads to a stable finite element formulation of the coupled problem. Instabilities might only occur if the beam finite elements become significantly shorter than the solid finite elements. However, as discussed in [55, 57], such BTS element size ratios are typically not relevant for the envisioned scope of applications.

4.3.1 Consistent positional coupling (BTSS-POS-CONS)

Inserting the finite element interpolations into the first term of (20) yields the discrete variation of the BTSS-POS-CONS

coupling constraints,

$$\begin{aligned} \delta W_{\lambda_r, h} = & \sum_{l=1}^{n_B} \sum_{j=1}^{n_\lambda} \delta \lambda_{r,j}^T \underbrace{\int_{\Gamma_{c,h}} \Phi_{r,j} \mathbf{H}_l \, ds}_{\mathbf{D}^{(j,l)}} \mathbf{x}_l^B \\ & - \sum_{k=1}^{n_\Gamma} \sum_{j=1}^{n_\lambda} \delta \lambda_{r,j}^T \underbrace{\int_{\Gamma_{c,h}} \Phi_{r,j} N_k \, ds}_{\mathbf{M}^{(j,k)}} \mathbf{I}^{3 \times 3} \mathbf{x}_k^S \\ & - \sum_{j=1}^{n_\lambda} \delta \lambda_{r,j}^T \underbrace{\int_{\Gamma_{c,h}} \Phi_{r,j} d_{c,0} \mathbf{n}_h \, ds}_{\mathbf{q}^{(j)}} \end{aligned} \quad (46)$$

Here, two local matrices with mass matrix-like structure can be identified: $\mathbf{D}^{(j,l)} \in \mathbb{R}^{3 \times 6}$ and $\mathbf{M}^{(j,k)} \in \mathbb{R}^{3 \times 3}$, i.e., the so-called mortar matrices. Furthermore, the abbreviation $\mathbf{q}^{(j)} \in \mathbb{R}^{3 \times 1}$ is introduced, referring to the integral of the surface normal distance weighted with the Lagrange multiplier shape function of the Lagrange multiplier node j . Again, inserting the finite element interpolations into the second term of (20) yields the discrete virtual work of the coupling forces,

$$\begin{aligned} \delta W_{C_r, h} = & \sum_{l=1}^{n_B} \sum_{j=1}^{n_\lambda} \left(\mathbf{D}^{(j,l)} \delta \mathbf{d}_l^B \right)^T \lambda_{r,j} \\ & - \sum_{k=1}^{n_\Gamma} \sum_{j=1}^{n_\lambda} \left(\mathbf{M}^{(j,k)} \delta \mathbf{d}_k^S \right)^T \lambda_{r,j} \\ & - \sum_{k=1}^{n_\Gamma} \sum_{j=1}^{n_\lambda} \left(\underbrace{\int_{\Gamma_{c,h}} d_{c,0} \delta \mathbf{n}_h \Phi_{r,j} \, ds}_{-\mathbf{Q}^{(j,k)} \delta \mathbf{d}_k^S} \right)^T \lambda_{r,j} \end{aligned} \quad (47)$$

where the abbreviation $\mathbf{Q}^{(j,k)} = -\frac{\partial \mathbf{q}^{(j)}}{\partial \mathbf{d}_k^S}$ is introduced. With equations (46) and (47) the discretized global virtual work of the coupling contributions reads

$$\delta \Pi_{\lambda_r, h} = \begin{bmatrix} \delta \mathbf{d}^S{}^T & \delta \mathbf{d}_r^B{}^T & \delta \lambda_r^T \end{bmatrix} \begin{bmatrix} (-\mathbf{M} + \mathbf{Q})^T \lambda_r \\ \mathbf{D}^T \lambda_r \\ \mathbf{D} \mathbf{x}^B - \mathbf{M} \mathbf{x}^S - \mathbf{q} \end{bmatrix}. \quad (48)$$

Here, $\mathbf{D} \in \mathbb{R}^{3n_\lambda \times 6n_B}$, $\mathbf{M} \in \mathbb{R}^{3n_\lambda \times 3n_\Gamma}$, $\mathbf{q} \in \mathbb{R}^{3n_\lambda \times 1}$ and $\mathbf{Q} \in \mathbb{R}^{3n_\lambda \times 3n_\Gamma}$ are the globally assembled matrices and vector of the previously defined local ones. The following residual vectors can be identified in (48)

$$\begin{bmatrix} \mathbf{r}_{c, \lambda_r}^S \\ \mathbf{r}_{c, \lambda_r}^B \\ \mathbf{r}_{c, \lambda_r} \end{bmatrix}_{\text{CONS}} = \begin{bmatrix} (-\mathbf{M} + \mathbf{Q})^T \lambda_r \\ \mathbf{D}^T \lambda_r \\ \mathbf{D} \mathbf{x}^B - \mathbf{M} \mathbf{x}^S - \mathbf{q} \end{bmatrix}. \quad (49)$$

Here, the abbreviations $\mathbf{r}_{c, \lambda_r}^S$ and $\mathbf{r}_{c, \lambda_r}^B$ are the coupling residual force vectors acting on the solid and beam degrees of freedom, respectively, and $\mathbf{r}_{c, \lambda_r}$ is the residual vector of the constraint equations. The residual vectors for the positional

coupling conditions are added to those of the uncoupled system (44). A linearization of the coupling residuum vectors with respect to the discrete degrees of freedom is required for the Newton–Raphson algorithm used to solve the nonlinear system of equations resulting from the discretization process. The linearization of the positional coupling contributions reads:

$$\begin{aligned} \text{Lin} \left(\begin{bmatrix} \mathbf{r}_{c, \lambda_r}^S \\ \mathbf{r}_{c, \lambda_r}^B \\ \mathbf{r}_{c, \lambda_r} \end{bmatrix}_{\text{CONS}} \right) = & \begin{bmatrix} \mathbf{0} \\ \mathbf{0} \\ \mathbf{r}_{c, \lambda_r} \end{bmatrix}_{\text{CONS}} \\ & + \begin{bmatrix} \mathbf{Q}_{ss} & \mathbf{0} & -\mathbf{M}^T + \mathbf{Q}^T \\ \mathbf{0} & \mathbf{0} & \mathbf{D}^T \\ -\mathbf{M} + \mathbf{Q} \mathbf{D} & \mathbf{0} & \mathbf{0} \end{bmatrix} \begin{bmatrix} \Delta \mathbf{d}^S \\ \Delta \mathbf{d}_r^B \\ \lambda_r \end{bmatrix}, \end{aligned} \quad (50)$$

where the abbreviation $\mathbf{Q}_{ss} = \frac{\partial (\mathbf{Q}^T \lambda_r)}{\partial \mathbf{d}^S}$ is introduced.

In practice, all integrals are numerically evaluated using segment-based integration along the beam centerline, which avoids integration over discontinuities, cf. [16, 55]. Each subsegment is integrated using Gauss–Legendre quadrature with a fixed number of integration points for all coupling terms, which is required to ensure conservation of linear and angular momentum, cf. Section 4.5.3. Segment-based integration yields an accurate numerical evaluation of the coupling integrals and allows for the resulting coupling scheme to pass patch test-like problems, cf. [55]. Furthermore, all derivatives explicitly stated in the discrete equations are evaluated using forward automatic differentiation (FAD), cf. [30], using the Sacado software package [49], which is part of the Trilinos project [60].

4.3.2 Forced reference configuration coupling (BTSS-POS-REF)

By neglecting the normal distance $d_{c,0}$, the BTSS-POS-REF variant of the positional coupling conditions (21) simplifies the coupling equations (17), such that the surface normal vector does not appear in the coupling equations anymore. The discrete coupling terms for the BTSS-POS-REF variant read

$$\begin{bmatrix} \mathbf{r}_{c, \lambda_r}^S \\ \mathbf{r}_{c, \lambda_r}^B \\ \mathbf{r}_{c, \lambda_r} \end{bmatrix}_{\text{REF}} = \begin{bmatrix} -\mathbf{M}^T \lambda_r \\ \mathbf{D}^T \lambda_r \\ \mathbf{D} \mathbf{x}^B - \mathbf{M} \mathbf{x}^S \end{bmatrix}. \quad (51)$$

It becomes clear, that the constraint equations in the reference configuration are only fulfilled if $\mathbf{D} \mathbf{x}^B - \mathbf{M} \mathbf{x}^S = \mathbf{0}$. Otherwise, this coupling variant leads to initial (coupling) stresses in the system. The influence of the initial stresses within the BTSS-POS-DISP variant is analyzed in Section 5. The

linearization of the coupling terms (51) reads

$$\text{Lin} \left(\begin{bmatrix} \mathbf{r}_{c,\lambda_r}^S \\ \mathbf{r}_{c,\lambda_r}^B \\ \mathbf{r}_{c,\lambda_r} \end{bmatrix}_{\text{REF}} \right) = \begin{bmatrix} \mathbf{0} \\ \mathbf{0} \\ \mathbf{r}_{c,\lambda_r} \end{bmatrix}_{\text{REF}} + \begin{bmatrix} \mathbf{0} & \mathbf{0} & -\mathbf{M}^T \\ \mathbf{0} & \mathbf{0} & \mathbf{D}^T \\ -\mathbf{M} & \mathbf{D} & \mathbf{0} \end{bmatrix} \begin{bmatrix} \Delta \mathbf{d}^S \\ \Delta \mathbf{d}_r^B \\ \lambda_r \end{bmatrix}. \quad (52)$$

4.3.3 Displacement coupling (BTSS-POS-DISP)

Another alternative positional coupling variant is the BTSS-POS-DISP variant (24). Therein, the normal distance between the beam and the solid surface is neglected and the displacements are directly coupled to each other. The discrete coupling terms for the BTSS-POS-DISP variant read:

$$\begin{bmatrix} \mathbf{r}_{c,\lambda_r}^S \\ \mathbf{r}_{c,\lambda_r}^B \\ \mathbf{r}_{c,\lambda_r} \end{bmatrix}_{\text{DISP}} = \begin{bmatrix} -\mathbf{M}^T \lambda_r \\ \mathbf{D}^T \lambda_r \\ \mathbf{D} \mathbf{d}^B - \mathbf{M} \mathbf{d}^S \end{bmatrix}. \quad (53)$$

In this case, the coupling constraints are fulfilled in the reference configuration and there are no initial stresses in the system. However, this variant violates conservation of angular momentum. Again, the influence of this violation within the BTSS-POS-DISP variant is analyzed in Section 5. The linearization of the coupling terms (53) reads

$$\text{Lin} \left(\begin{bmatrix} \mathbf{r}_{c,\lambda_r}^S \\ \mathbf{r}_{c,\lambda_r}^B \\ \mathbf{r}_{c,\lambda_r} \end{bmatrix}_{\text{DISP}} \right) = \begin{bmatrix} \mathbf{0} \\ \mathbf{0} \\ \mathbf{r}_{c,\lambda_r} \end{bmatrix}_{\text{DISP}} + \begin{bmatrix} \mathbf{0} & \mathbf{0} & -\mathbf{M}^T \\ \mathbf{0} & \mathbf{0} & \mathbf{D}^T \\ -\mathbf{M} & \mathbf{D} & \mathbf{0} \end{bmatrix} \begin{bmatrix} \Delta \mathbf{d}^S \\ \Delta \mathbf{d}_r^B \\ \lambda_r \end{bmatrix}. \quad (54)$$

Remark 4.1 A very similar problem occurs for surface-to-surface mesh tying problems in the case of general curved interfaces. To guarantee conservation of angular momentum a mesh initialization procedure is performed, cf. [43]. The mesh initialization slightly relocates the reference position of the slave nodes (in the case of BTS problems, the beam nodes) \mathbf{X}^B , such that the (non-linear) condition $\mathbf{D}\mathbf{X}^B - \mathbf{M}\mathbf{X}^S = \mathbf{0}$ is fulfilled (in [43], the non-linear mesh initialization is not solved exactly, but approximated via a single linear step). For the presented BTSS-POS method, such a mesh initialization would mean that both presented simplifications BTSS-POS-REF and BTSS-POS-DISP are identical. However, in the surface-to-surface case the space continuous interfaces are usually matching, thus the mesh initialization of the discretized system only marginally affects the overall solution. This is not the case for BTSS coupling problems. For example, in many situations it is sensible for the beam centerline to be offset of the coupling surface in surface

normal direction. In such cases, the mesh initialization procedure of the beam reference configuration might lead to a drastically different system behavior.

Remark 4.2 If the discretized beam centerline lies exactly on the discretized solid surface, the three presented variants of the global system equations (50), (52) and (54) are identical, i.e., $\mathbf{Q} = \mathbf{0}$ and $\mathbf{D}\mathbf{X}^B - \mathbf{M}\mathbf{X}^S = \mathbf{0}$. However, with the employed Lagrange polynomial interpolation for the solid finite elements and the third-order Hermitian interpolation for the beam finite elements, a matching mesh for beam and solid surface discretizations is only possible in case of planar solid surfaces. Furthermore, in this special case, the positional surface coupling variants would also be equal to the BTSV-POS method [55], as the problem can also be interpreted as a volume coupling problem, where the beam is directly embedded at the boundary of the solid volume, i.e., the solid surface. There, the beam would lie at a face of the solid (volume) finite element parameter space, i.e., the limit case for BTSV coupling.

4.4 Mortar-type coupling of rotations (BTSS-ROT)

The rotational coupling between beam cross-section and solid surface (BTSS-ROT) is entirely based on the BTSV-ROT coupling method presented in [57]. Therein, a mortar-type approach is employed to weakly enforce the rotational coupling constraints (28). The linearization of the global residuum vectors for rotational coupling reads,

$$\text{Lin} \left(\begin{bmatrix} \mathbf{r}_{c,\lambda_\theta}^S \\ \mathbf{r}_{c,\lambda_\theta}^B \\ \mathbf{r}_{c,\lambda_\theta} \end{bmatrix} \right) = \begin{bmatrix} \mathbf{0} \\ \mathbf{0} \\ \mathbf{r}_{c,\lambda_\theta} \end{bmatrix} + \begin{bmatrix} \mathbf{Q}_{ss}^{\text{ROT}} & \mathbf{Q}_{s\theta}^{\text{ROT}} & \mathbf{Q}_{s\lambda_\theta}^{\text{ROT}} \\ \mathbf{Q}_{\theta s}^{\text{ROT}} & \mathbf{Q}_{\theta\theta}^{\text{ROT}} & \mathbf{Q}_{\theta\lambda_\theta}^{\text{ROT}} \\ \mathbf{Q}_{\lambda_\theta s}^{\text{ROT}} & \mathbf{Q}_{\lambda_\theta\theta}^{\text{ROT}} & \mathbf{0} \end{bmatrix} \begin{bmatrix} \Delta \mathbf{d}^S \\ \Delta \mathbf{d}_\theta^B \\ \lambda_\theta \end{bmatrix}. \quad (55)$$

Here, $\mathbf{Q}_{(\cdot)(\cdot)}^{\text{ROT}}$ are the rotational coupling matrices and λ_θ are the Lagrange multipliers enforcing the rotational coupling constraints. Furthermore, $\mathbf{r}_{c,\lambda_\theta}^S$ and $\mathbf{r}_{c,\lambda_\theta}^B$ are the rotational coupling residual force vectors associated with the solid and beam degrees of freedom, respectively, and $\mathbf{r}_{c,\lambda_\theta}$ is the residual vector of the rotational constraint equations. For the derivation of the rotational coupling terms the interested reader is referred to our previous publication [57, Section 6.3]

4.5 Combined mortar-type coupling and penalty regularization (BTSS-FULL)

4.5.1 Coupling equations

In this section the global system for the BTSS-FULL problem is assembled and subsequently regularized. The BTSS-FULL problem consists of the following individual parts:

the uncoupled beam and solid problem, the positional coupling (BTSS-POS) and the rotational coupling (BTSS-ROT). In Section 4.3 three different variants of BTSS-POS are presented: BTSS-POS-CONS, BTSS-POS-REF and BTSS-POS-DISP. Depending on the employed variant, the corresponding BTSS-FULL problem is referred to as BTSS-FULL-CONS, BTSS-FULL-REF and BTSS-FULL-DISP. BTSS-FULL-CONS is the most general of the presented variants, i.e., the equations for the other variants are more or less simplifications thereof. In Section 5, BTSS-FULL-CONS will be identified as the superior variant with respect to the accuracy of the results. Therefore, and for the sake of brevity, the following derivations are only presented for the fully coupled and consistent BTSS-FULL-CONS variant. To improve readability, the subscript $(\cdot)_{\text{CONS}}$ will be omitted going further.

Combining the individual contributions to the BTSS-FULL-CONS problem, i.e., the uncoupled system (44), the positional BTSS-POS-CONS coupling terms (50) and the rotational BTSS-ROT coupling terms (55), yields the following global system of equations:

$$\begin{bmatrix} \mathbf{K}_{ss}^S + \mathbf{Q}_{ss} + \mathbf{Q}_{ss}^{\text{ROT}} & \mathbf{0} & \mathbf{Q}_{s\theta}^{\text{ROT}} & -\mathbf{M}^T + \mathbf{Q}^T & \mathbf{Q}_{s\lambda_\theta}^{\text{ROT}} \\ \mathbf{0} & \mathbf{K}_{rr}^B & \mathbf{0} & \mathbf{D}^T & \mathbf{0} \\ \mathbf{Q}_{\theta s}^{\text{ROT}} & \mathbf{0} & \mathbf{K}_{\theta\theta}^B + \mathbf{Q}_{\theta\theta}^{\text{ROT}} & \mathbf{0} & \mathbf{Q}_{\theta\lambda_\theta}^{\text{ROT}} \\ -\mathbf{M} + \mathbf{Q} & \mathbf{D} & \mathbf{0} & \mathbf{0} & \mathbf{0} \\ \mathbf{Q}_{\lambda_\theta s}^{\text{ROT}} & \mathbf{0} & \mathbf{Q}_{\lambda_\theta\theta}^{\text{ROT}} & \mathbf{0} & \mathbf{0} \end{bmatrix} \cdot \begin{bmatrix} \Delta \mathbf{d}^S \\ \Delta \mathbf{d}_r^B \\ \Delta \mathbf{d}_\theta^B \\ \lambda_r \\ \lambda_\theta \end{bmatrix} = \begin{bmatrix} -\mathbf{r}^S \\ -\mathbf{r}_r^B \\ -\mathbf{r}_\theta^B \\ -\mathbf{r}_{c,\lambda_r} \\ -\mathbf{r}_{c,\lambda_\theta} \end{bmatrix}. \quad (56)$$

4.5.2 Penalty regularization

Enforcing the coupling conditions with Lagrange multipliers results in a mixed formulation, i.e., the Lagrange multipliers are additional global unknowns. This leads to a saddle point-type structure of the global system (56). A direct solution of this global system introduces certain drawbacks, e.g., an increased system size and possible linear solver issues due to the saddle point-type structure. A weighted penalty regularization has proven to be an efficient and reasonably accurate approach to circumvent the aforementioned drawbacks for BTS coupling problems, cf. [55, 57]. Therefore, the resulting global system (56) will also be approximated with a penalty regularization. For the rotational coupling constraints the same penalty relaxation as in [57] will be employed, i.e., $\lambda_\theta = \epsilon_\theta \mathbf{V}_{\lambda_\theta}^{-1} \mathbf{r}_{c,\lambda_\theta}$. Therein, $\epsilon_\theta \in \mathbb{R}^+$ is a scalar penalty parameter and $\mathbf{V}_{\lambda_\theta}$ is a diagonal scaling matrix to account for the non-uniform weighting of the constraint

equations. A similar relaxation is employed for the positional coupling constraints,

$$\lambda_r = \epsilon_r \mathbf{V}_r^{-1} \mathbf{r}_{c,\lambda_r}. \quad (57)$$

Again, $\epsilon_r \in \mathbb{R}^+$ is a scalar penalty parameter and \mathbf{V}_r is a global diagonal scaling matrix. The global scaling matrix is assembled from the nodal scaling matrices $\kappa_r^{(i,i)}$ for Lagrange multiplier node i , cf. [55, 57], i.e.,

$$\kappa_r^{(i,i)} = \int_{\Gamma_{c,h}} \Phi_{r,j} \, ds \, \mathbf{1}^{3 \times 3}. \quad (58)$$

The penalty regularization introduces two additional system parameters, ϵ_r and ϵ_θ . This leaves the important question on how to choose these two parameters. Obviously, choosing the penalty parameters too high can lead to an ill-conditioned system matrix and subsequent issues with the numerical solution procedure, as well as to contact locking effects [55]. Moreover, also from a mechanical point of view, an infinitely large penalty parameter is not desirable. This is because in the real physical problem the beam cross-section comes with a certain deformability. However, the employed beam theory introduces the assumption of rigid cross-sections. Therefore, the penalty parameter is no longer a pure mathematical tool of constraint enforcement, but it also has a physical meaning, i.e., it represents the beam cross-section stiffness. Similar observations can be made in the case of beam-to-beam contact, cf. [34]. Going further, one could define the penalty parameter based on continuum mechanical analysis of the cross-section deformability and stiffness. However, since our primary interest is the regularization of (56), the following rule of thumb for choosing the two penalty parameters can be given: the positional penalty parameter should be in the range of the Young's modulus of the beam, i.e., $\epsilon_r \approx E_B$, and the rotational parameter should be in the range of the Young's modulus of the beam scaled with the square of the cross-section radius, i.e., $\epsilon_\theta \approx E_B R^2$. In practice, this does not lead to an unphysically large violation of the coupling constraints, and contact locking has not been observed in combination with a linear interpolation of the Lagrange multiplier field, cf. [55].

The relaxation of the penalty constraints defines the Lagrange multipliers as functions of the displacements, i.e., they are no longer independent degrees of freedom of the system and can be removed from the global system of equations (56):

$$\begin{bmatrix} \mathbf{A}_{ss} & \mathbf{A}_{sr} & \mathbf{A}_{s\theta} \\ \mathbf{A}_{rs} & \mathbf{A}_{rr} & \mathbf{A}_{r\theta} \\ \mathbf{A}_{\theta s} & \mathbf{A}_{\theta r} & \mathbf{A}_{\theta\theta} \end{bmatrix} \begin{bmatrix} \Delta \mathbf{d}^S \\ \Delta \mathbf{d}_r^B \\ \Delta \mathbf{d}_\theta^B \end{bmatrix} = \begin{bmatrix} \mathbf{B}_s \\ \mathbf{B}_r \\ \mathbf{B}_\theta \end{bmatrix}. \quad (59)$$

Therein, the following abbreviations have been introduced for improved readability:

$$\begin{aligned}
\mathbf{A}_{ss} &= \mathbf{K}_{ss}^S + \mathbf{Q}_{ss} + \mathbf{Q}_{ss}^{\text{ROT}} \\
&\quad + \epsilon_r (-\mathbf{M} + \mathbf{Q})^T \mathbf{V}_r^{-1} (-\mathbf{M} + \mathbf{Q}) \\
&\quad + \epsilon_\theta \mathbf{Q}_{s\lambda_\theta}^{\text{ROT}} \mathbf{V}_{\lambda_\theta}^{-1} \mathbf{Q}_{\lambda_\theta s}^{\text{ROT}} \\
\mathbf{A}_{sr} &= \epsilon_r (-\mathbf{M} + \mathbf{Q})^T \mathbf{V}_r^{-1} \mathbf{D} \\
\mathbf{A}_{s\theta} &= \mathbf{Q}_{s\theta}^{\text{ROT}} + \epsilon_\theta \mathbf{Q}_{s\lambda_\theta}^{\text{ROT}} \mathbf{V}_{\lambda_\theta}^{-1} \mathbf{Q}_{\lambda_\theta\theta}^{\text{ROT}} \\
\mathbf{A}_{rs} &= \epsilon_r \mathbf{D}^T \mathbf{V}_r^{-1} (-\mathbf{M} + \mathbf{Q}) \\
\mathbf{A}_{rr} &= \mathbf{K}_{rr}^B + \epsilon_r \mathbf{D}^T \mathbf{V}_r^{-1} \mathbf{D} \\
\mathbf{A}_{r\theta} &= \mathbf{K}_{r\theta}^B \\
\mathbf{A}_{\theta s} &= \mathbf{Q}_{\theta s}^{\text{ROT}} + \epsilon_\theta \mathbf{Q}_{\theta\lambda_\theta}^{\text{ROT}} \mathbf{V}_{\lambda_\theta}^{-1} \mathbf{Q}_{\lambda_\theta s}^{\text{ROT}} \\
\mathbf{A}_{\theta r} &= \mathbf{K}_{\theta r}^B \\
\mathbf{A}_{\theta\theta} &= \mathbf{K}_{\theta\theta}^B + \mathbf{Q}_{\theta\theta}^{\text{ROT}} + \epsilon_\theta \mathbf{Q}_{\theta\lambda_\theta}^{\text{ROT}} \mathbf{V}_{\lambda_\theta}^{-1} \mathbf{Q}_{\lambda_\theta\theta}^{\text{ROT}} \\
\mathbf{B}_s &= -\mathbf{r}^S - \epsilon_r (-\mathbf{M} + \mathbf{Q})^T \mathbf{V}_r^{-1} \mathbf{r}_{c,\lambda_r} \\
&\quad - \epsilon_\theta \mathbf{Q}_{s\lambda_\theta}^{\text{ROT}} \mathbf{V}_{\lambda_\theta}^{-1} \mathbf{r}_{c,\lambda_\theta} \\
\mathbf{B}_r &= -\mathbf{r}_r^B - \epsilon_r \mathbf{D}^T \mathbf{V}_r^{-1} \mathbf{r}_{c,\lambda_r} \\
\mathbf{B}_\theta &= -\mathbf{r}_\theta^B - \epsilon_\theta \mathbf{Q}_{\theta\lambda_\theta}^{\text{ROT}} \mathbf{V}_{\lambda_\theta}^{-1} \mathbf{r}_{c,\lambda_\theta}.
\end{aligned} \tag{60}$$

4.5.3 Conservation properties

In this section, the proposed BTSS-FULL-CONS scheme shall be analyzed with respect to conservation of linear momentum and angular momentum. For the rotational coupling constraints conservation of angular momentum (there is no linear momentum introduced by the rotational coupling constraints) is shown in [57]. Therefore, it is sufficient to analyze the BTSS-POS-CONS scheme in this section.

In the context of surface-to-surface problems this has been discussed in detail, e.g., [42–45]. For surface-to-surface coupling (mesh tying) problems it has been shown that conservation of linear momentum and angular momentum is satisfied by the semi-discrete mesh tying formulation, cf. [43]. However, the proposed mixed-dimensional BTSS-POS-CONS scheme differs in two important aspects from classical surface-to-surface coupling problems: (i) The coupling constraints are formulated with the current positions instead of the displacements, and, more importantly, contain the surface normal vector. (ii) The nodal degrees of freedom for the beam nodes contain the positions as well as the centerline tangents. Therefore, a discussion on conservation of linear momentum and angular momentum of the BTSS-POS-CONS variant is warranted. In the following considerations the BTSS-POS-CONS is analyzed, as the implications for BTSS-POS-REF can be directly obtained by applying the respective simplifications. In the case of BTSS-POS-DISP, it is shown in Section 4.3.2 that already the space continuous coupling terms do not conserve angular momentum.

As discussed in [43], conservation of linear momentum can be guaranteed if the discretized virtual work of the coupling forces vanishes for a constant virtual displacement $\delta \underline{\mathbf{u}} \neq \mathbf{0}$. In that case, the nodal displacement weighting functions become $\delta \underline{\mathbf{d}}_k^S = \delta \underline{\mathbf{u}}$, $k = 1, \dots, n_\Gamma$ and $\delta \underline{\mathbf{d}}_l^{B,r} = \delta \underline{\mathbf{u}}$, $l = 1, \dots, n_B$. Since the virtual displacement is constant, the variation of the beam centerline tangents vanishes, i.e., $\delta \underline{\mathbf{d}}_l^{B,t} = \mathbf{0}$, $l = 1, \dots, n_B$. Insertion into (47) yields

$$\begin{aligned}
&\sum_{j=1}^{n_\lambda} \left(\sum_{l=1}^{n_B} \left(\mathbf{D}^{(j,l)} \begin{bmatrix} \delta \underline{\mathbf{u}} \\ \mathbf{0} \end{bmatrix} \right)^T - \sum_{k=1}^{n_\Gamma} \left(\mathbf{M}^{(j,k)} \delta \underline{\mathbf{u}} \right)^T \right. \\
&\quad \left. - \int_{\Gamma_{c,h}} d_{c,0} \delta \underline{\mathbf{n}}_h \Phi_{r,j} ds \right) \underline{\lambda}_{r,j} = 0.
\end{aligned} \tag{61}$$

The variation of the surface normal vector vanishes for a constant virtual displacement field, i.e., $\delta \underline{\mathbf{n}}_h = \mathbf{0}$. Furthermore, since $\delta \underline{\mathbf{u}}$ is non-zero, the condition (61) is only satisfied if

$$\left(\sum_{l=1}^{n_B} \int_{\Gamma_{c,h}} \Phi_{r,j} H_l^r ds - \sum_{k=1}^{n_\Gamma} \int_{\Gamma_{c,h}} \Phi_{r,j} N_k ds \right) \underline{\lambda}_{r,j} = \mathbf{0}. \tag{62}$$

With the partition of unity property of H_l^r and N_k , i.e., $\sum_{l=1}^{n_B} H_l^r = 1$ and $\sum_{k=1}^{n_\Gamma} N_k = 1$, the condition for conservation of linear momentum further simplifies to

$$\sum_{j=1}^{n_\lambda} \left(\int_{\Gamma_{c,h}} \Phi_{r,j} ds - \int_{\Gamma_{c,h}} \Phi_{r,j} ds \right) = 0. \tag{63}$$

Obviously this property is fulfilled if the integrals are evaluated exactly. In the case of numerical integration the property is fulfilled if the same numerical integration procedure is used for both integrals. At this point it is important to point out that the two integrals originally arise from the evaluation of $\mathbf{D}^{(j,l)}$ and $\mathbf{M}^{(j,k)}$. As mentioned in Section 4.3 a segment-based integration with a fixed number of Gauss-points is performed, therefore, the discrete BTSS-POS-CONS scheme exactly conserves linear momentum.

In a similar fashion, conservation of angular momentum can be guaranteed, if the virtual work of the coupling forces vanishes for a constant virtual rotation $\delta \underline{\phi} \neq \mathbf{0}$ (for simplicity, the origin is assumed to be the center of the virtual rotation). With that assumption, the nodal virtual displacements of solid and beam are $\delta \underline{\mathbf{d}}_k^S = \delta \underline{\phi} \times \underline{\mathbf{x}}_k^S$, $k = 1, \dots, n_\Gamma$ and $\delta \underline{\mathbf{d}}_l^{B,r} = \delta \underline{\phi} \times \underline{\mathbf{r}}_l^B$, $l = 1, \dots, n_B$. The variation of the nodal beam tangent vectors reads $\delta \underline{\mathbf{d}}_l^{B,t} = \delta \underline{\phi} \times \underline{\mathbf{t}}_l^B$, $l =$

1, ..., n_B , cf. [35]. Insertion into (47) yields

$$\begin{aligned} \sum_{j=1}^{n_\lambda} \left[\sum_{l=1}^{n_B} \left((\delta \underline{\phi} \times \underline{\mathbf{r}}_l^B)^T \int_{\Gamma_{c,h}} \Phi_{r,j} H_l^r ds \right. \right. \\ \left. \left. + (\delta \underline{\phi} \times \underline{\mathbf{t}}_l^B)^T \int_{\Gamma_{c,h}} \Phi_{r,j} H_l^t ds \right) \right. \\ \left. - \sum_{k=1}^{n_\Gamma} (\delta \underline{\phi} \times \underline{\mathbf{x}}_k^S)^T \int_{\Gamma_{c,h}} \Phi_{r,j} N_k ds \right. \\ \left. - \int_{\Gamma_{c,h}} d_{c,0} \delta \underline{\mathbf{n}}_h^T \Phi_{r,j} ds \right] \underline{\lambda}_{r,j} = 0. \end{aligned} \quad (64)$$

In the case of a constant virtual rotation, the variation of the normal vector can be expressed as $\delta \underline{\mathbf{n}}_h = \delta \underline{\phi} \times \underline{\mathbf{n}}_h$. Since $\delta \underline{\phi}$ is non-zero, the condition (64) is only fulfilled if

$$\begin{aligned} \sum_{j=1}^{n_\lambda} \left[\sum_{l=1}^{n_B} \left(\int_{\Gamma_{c,h}} \Phi_{r,j} H_l^r ds \underline{\mathbf{r}}_l^B + \int_{\Gamma_{c,h}} \Phi_{r,j} H_l^t ds \underline{\mathbf{t}}_l^B \right) \right. \\ \left. \underbrace{\hspace{10em}}_{\mathbf{D}^{(j,l)} \mathbf{x}_l^B} \right. \\ \left. - \sum_{k=1}^{n_\Gamma} \int_{\Gamma_{c,h}} \Phi_{r,j} N_k ds \mathbf{I}^{3 \times 3} \underline{\mathbf{x}}_k^S \right. \\ \left. \underbrace{\hspace{10em}}_{\mathbf{M}^{(j,k)T}} \right. \\ \left. - \int_{\Gamma_{c,h}} d_{c,0} \underline{\mathbf{n}}_h \Phi_{r,j} ds \right] \times \underline{\lambda}_{r,j} = 0. \end{aligned} \quad (65)$$

This condition can be reformulated and written in global form

$$\mathbf{D} \mathbf{x}^B - \mathbf{M} \mathbf{x}^S - \mathbf{q} = \mathbf{0}. \quad (66)$$

These are simply the coupling constraints for BTSS-POS-CONS, i.e., if the coupling constraints, cf. last row in (48), are fulfilled, the coupling scheme preserves angular momentum. In the present work, the coupling constraints are enforced with a node-wise weighted penalty regularization, which results in a slight violation of the coupling constraints. However, the resulting regularized problem still preserves angular momentum. To demonstrate this, we state the penalty regularization for a Lagrange multiplier at node j :

$$\begin{aligned} \underline{\lambda}_{r,j} = \epsilon_r \left(\int_{\Gamma_{c,h}} \Phi_{r,j} ds \mathbf{I}^{3 \times 3} \right)^{-1} \\ \left(\sum_{l=1}^{n_B} \mathbf{D}^{(j,l)} \mathbf{x}_l^B - \sum_{k=1}^{n_\Gamma} \mathbf{M}^{(j,k)} \underline{\mathbf{x}}_k^S - \mathbf{q}^{(j)} \right). \end{aligned} \quad (67)$$

When inserting (67) into (65) it is obvious that the condition for conservation of angular momentum is also fulfilled for the regularized problem, as the cross product of two parallel vectors vanishes.

4.6 Extended beam-to-solid volume coupling

The main difference between the proposed BTSS-POS-CONS coupling procedure and the BTSV-POS method, cf. [55], is a term accounting for the normal distance between the beam and the solid surface. The discretization of this term introduces rather complex coupling terms, which require the evaluation of an averaged surface normal field. An alternative to the BTSS-POS-CONS method is to use an extended version of the BTSV-POS scheme proposed in [55], which shall be denoted as the *extended* positional beam-to-solid volume coupling (BTSV-POS-X) scheme in the following. The idea of this BTSV-POS-X scheme is to simply project points on the beam centerline to an extended solid parameter space, i.e., projections that lie outside of the solid volume are still admissible. Thus, no closest point projection with the surface normal field is required. This is exemplarily illustrated in Figure 8. The point $\underline{\mathbf{p}}$ is projected to the parameter space of the solid finite element (e), and although the ξ_2 coordinate of the projection point lies outside of the solid finite element domain the projection will still be used in the evaluation of \mathbf{M} . There are no coupling terms dependent on the surface normal distance in this case, i.e., the resulting linearized system of equations is equal to (52) and (54). At first glance this approach might seem very appealing as there is no need for evaluating the surface normal vector and its derivatives. Furthermore, basically the same implementation as in BTSV-POS problems can be used. However, there are two significant drawbacks of this approach: (i) The projection of the beam centerline points onto the solid surface is highly dependent on the solid finite element mesh. Figure 9 illustrates cases where the BTSV-POS-X method fails. In Figure 9(a) the solid finite elements are distorted in negative normal direction of the coupling surface, such that a unique projection is not possible in the shaded areas. (ii) The BTSV-POS-X method only works well for grid-like hexahedral meshes of the solid surface, unstructured hexahedral meshes or tetrahedral meshes lead to problems due to non-unique projections, cf. Figure 9(b). Additionally, the proposed BTSS-POS-CONS method can be directly applied to structural models using shell finite elements, whereas the BTSV-POS-X method requires that the solid is discretized with 3D solid finite elements. Therefore, the BTSV-POS-X method will not be investigated further in this contribution.

5 Examples

The following numerical examples are set up using the open source beam finite element pre-processor MeshPy [56] and are simulated with the in-house parallel multi-physics research code BACI [2].

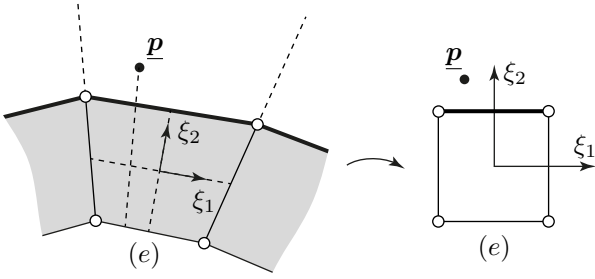


Fig. 8 Projection of point \underline{p} to the parameter space of the solid finite element (e) with BTSV-POS-X. For illustrative purposes a 2D example is shown.

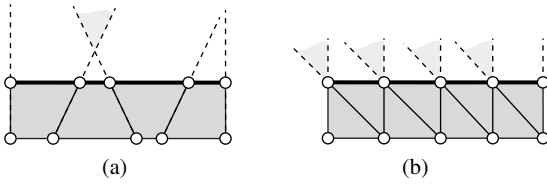


Fig. 9 Problematic cases for BTSV-POS-X. (a) Distorted elements in negative normal direction of the solid surface. (b) General tetrahedral mesh. Gray areas indicate where a projection to the solid surface fails. For illustrative purposes a 2D example is shown.

5.1 Constant stress transfer

In this first example the ability of the BTSS-FULL coupling method to transfer a constant stress state is investigated. This example is inspired by classical patch tests for solid mechanics, cf. [58]. Similar examples are presented in [55] for the BTSV-POS method and in [57] for the BTSV-FULL method. Figure 10 illustrates the problem setup, which consists of a solid block Ω^S ($E_S = 1 \text{ N/m}^2$, $\nu_S = 0$) with the dimensions $1 \text{ m} \times 1 \text{ m} \times 1.2 \text{ m}$. The center of the bottom face is located at the origin of the coordinate system. No external loads are applied to the solid and the bottom face is fixed in all spatial directions. At the top face the solid surface is coupled to two beams Ω_{B1} and Ω_{B2} ($R = 0.05 \text{ m}$, $E_B = 100 \text{ N/m}^2$, $\nu_B = 0$). The two beams share the same spatial position and are loaded with opposing line loads in \underline{e}_3 direction. The magnitude of the line loads is $t = 0.025 \text{ N/m}$. Note that this verification example is designed in a manner such that the two beams do not interact directly, e.g., via mechanical contact interaction, all loads are transferred through the solid domain via the BTSS-FULL coupling method. For the space continuous problem, the coupling forces resulting from two identical beams loaded with opposing line loads exactly balance each other, i.e., the net coupling force transferred to the solid surface vanishes and, thus, the analytical solution for the displacement field of the beams and the solid is $\underline{u} = \underline{\mathbf{0}}$. This example shall verify the ability of the three BTSS-FULL variants proposed in Section 2.5, i.e., BTSS-FULL-CONS, BTSS-FULL-REF and BTSS-FULL-DISP, to exactly represent this analytical solution using an arbitrary

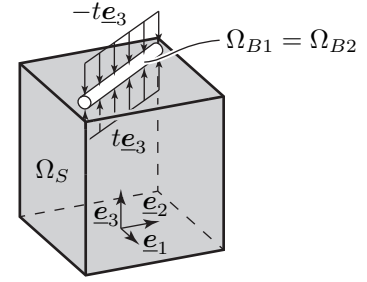


Fig. 10 Constant stress transfer – problem setup. The two beams Ω_{B1} and Ω_{B2} occupy the same spatial position.

trarily coarse discretization, i.e., the ability of the coupling method to transfer a constant stress state across non-matching mixed-dimensional interface meshes.

The solid block is discretized with first- and second-order hexahedral finite elements (*hex8*, *hex20* and *hex27*) as well as first- and second order tetrahedral finite elements (*tet4* and *tet10*). The beams $B1$ and $B2$ are discretized with 5 and 7 Simo–Reissner beam finite elements, respectively. This results in a non-matching mixed-dimensional interface discretization between the beams and the solid. The Lagrange multipliers for positional and rotational coupling are discretized using first-order Lagrange polynomials and regularized using penalty parameters of $\epsilon_r = 100 \text{ N/m}^2$ and $\epsilon_\theta = 0.1 \text{ Nm/m}$. The results for various coupling variants and *hex8* elements are illustrated in Figure 11. It can be seen that for all considered variants, the second Piola-Kirchhoff stress S_{33} in the solid and the curvature κ in the beam elements are zero up to machine precision, thus exactly representing the analytical solution. However, the displacement of the two beams in the BTSS-FULL-REF variant does not vanish, as the beam centerline is forced to lie on the solid surface, i.e., in this example the beams exhibit an offset in negative \underline{e}_3 -direction by a distance of R . The results of the constant stress transfer test for the various solid element types are visualized in Figure 12. There, the coupling is realized with the BTSS-FULL-CONS variant. It can be seen that for all considered solid element types, the stress in the solid and the curvature in the beam match the analytical solution up to machine precision. This illustrates that the BTSS-FULL-CONS coupling variant is able to exactly represent a constant stress state between a straight beam and a planar solid surface for general non-matching discretizations. The results obtained with BTSS-FULL-DISP exactly match the results obtained with BTSS-FULL-CONS. In case of the BTSS-FULL-REF variant, the beams displacement is not zero, but the constant stress state can still be transferred exactly.

To make the constant stress transfer test more demanding, the previously presented example is now modified to account for a curved surface contour of the solid described by the position field $\underline{\mathbf{X}}_S = i\underline{e}_1 + j\underline{e}_2 + f(i, j)\underline{e}_3$ for $i, j \in [-0.5, 0.5]$, with $f(i, j) = \frac{5}{4} - i^2 - j^2$. The centerlines of the two beams

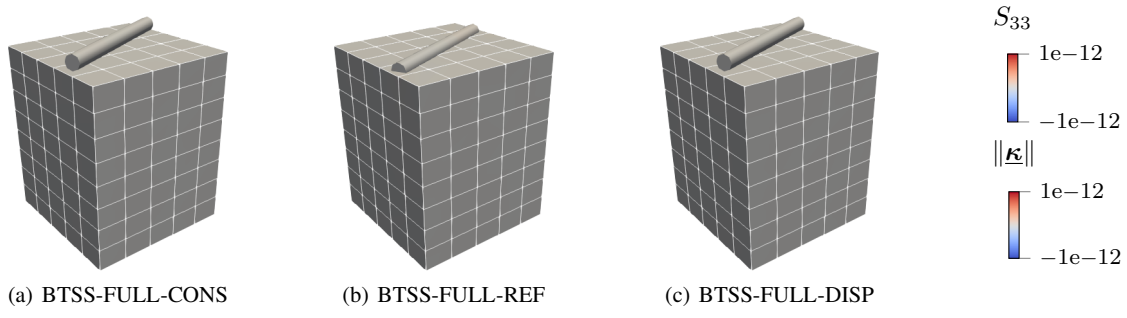


Fig. 11 Constant stress transfer – results for straight beams and various coupling variants. The solids are discretized with *hex8* solid finite elements. The second Piola-Kirchhoff stress S_{33} is shown in the solid and the curvature κ at the middle of each beam element. Note that the two beams Ω_{B1} and Ω_{B2} occupy the same spatial domain in the undeformed reference configuration. The gray color in the contour plot indicates a zero value up to machine precision.

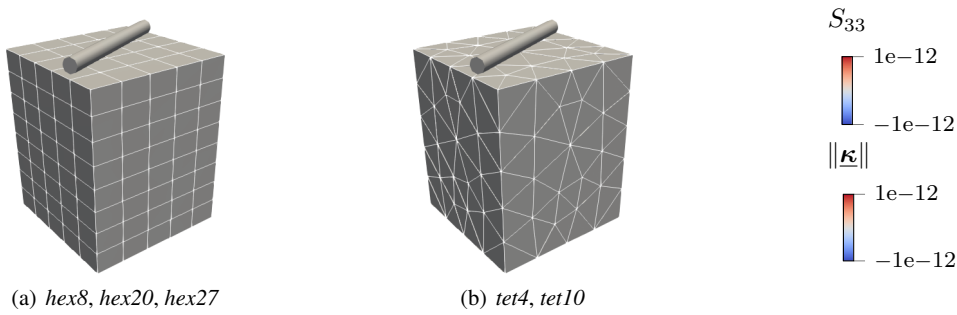


Fig. 12 Constant stress transfer – results for straight beams and various solid finite element discretizations. The coupling is modeled with the BTSS-FULL-CONS coupling variant. The second Piola-Kirchhoff stress S_{33} is shown in the solid and the curvature κ at the middle of each beam element. Note that the two beams Ω_{B1} and Ω_{B2} occupy the same spatial domain in the undeformed reference configuration. The gray color in the contour plot indicates a zero value up to machine precision.

are offset by the beam radius in surface normal direction. Otherwise, all parameters are the same as in the previous example. Because of the specific choice of surface curvature, the employed beam centerline interpolation with third-order Hermitian polynomials is not able to exactly represent the space continuous reference geometry of the beam centerline. This results in a discretization error of the beam centerline interpolation and slightly different arc lengths of the two beams. In order for the resultants of the two line loads to still be in equilibrium with each other, the load t on beam $B2$ is scaled with a factor of 0.9995346 to account for the different beam lengths. Figure 13 illustrates the results of the constant stress transfer test for the curved solid surface and the various coupling variants. It can clearly be seen that the results for BTSS-FULL-REF do not match the analytical solution. This is because the beam is forced to lie on the solid surface. In case of the planar coupling surface this could be achieved by a rigid body translation of the beams onto the solid surface. However, in case of the curved solid surface, a rigid body translation of the beams can not fulfill the positional coupling equations for BTSS-FULL-REF. This also requires a deformation of the beams and the solid, and thus results in a failing constant stress transfer test. Figure 14 illustrates the results for the BTSS-FULL-CONS variant in

combination with various solid finite element types. Note the different scaling of the contour plots in Figure 13 compared to Figure 14. It can be observed that even for the BTSS-FULL-CONS (and also the BTSS-FULL-DISP) variant, the analytical solution is not reproduced up to machine precision as the results show a non-vanishing stress state in the solid and a non-vanishing curvature in the beams. However, these non-zero stress and curvature values, respectively, are introduced by the discretization error of the initial geometry, i.e., the inability of the beam finite elements to exactly represent the curvature of the initial geometry, and are orders of magnitude smaller than the discretization errors associated with deformation states in typical application scenarios (and the error introduced by the BTSS-FULL-REF variant). It can be concluded that the discretization error for arbitrarily curved beam centerlines within the BTSS-FULL-CONS and BTSS-FULL-DISP methods can be neglected as compared to the overall discretization error.

5.2 Half-pipe with helix-shaped beam

In this example, a helix-shaped beam is coupled to the outer surface of a solid half-pipe, cf. Figure 15. This example is

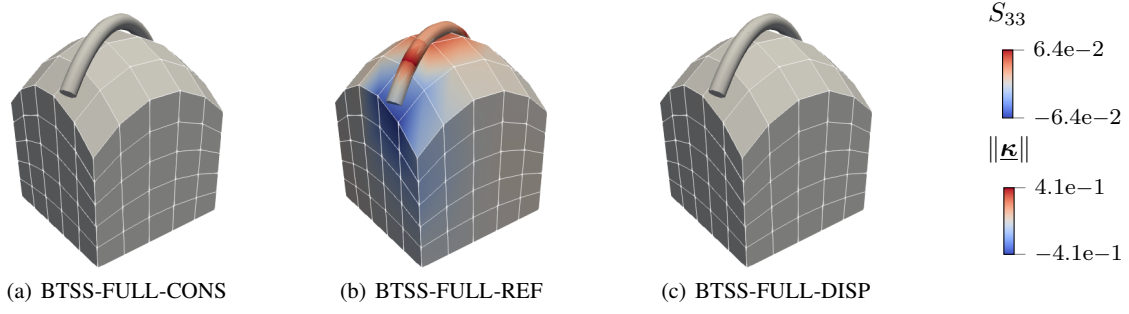


Fig. 13 Constant stress transfer – results for curved beams and various coupling variants. The solids are discretized with *hex8* solid finite elements. The second Piola-Kirchhoff stress S_{33} is shown in the solid and the curvature κ at the middle of each beam element. Note that the two beams Ω_{B1} and Ω_{B2} occupy the same spatial domain in the undeformed reference configuration. In (a) and (c) the gray color in the contour plot indicates a zero value up to machine precision.

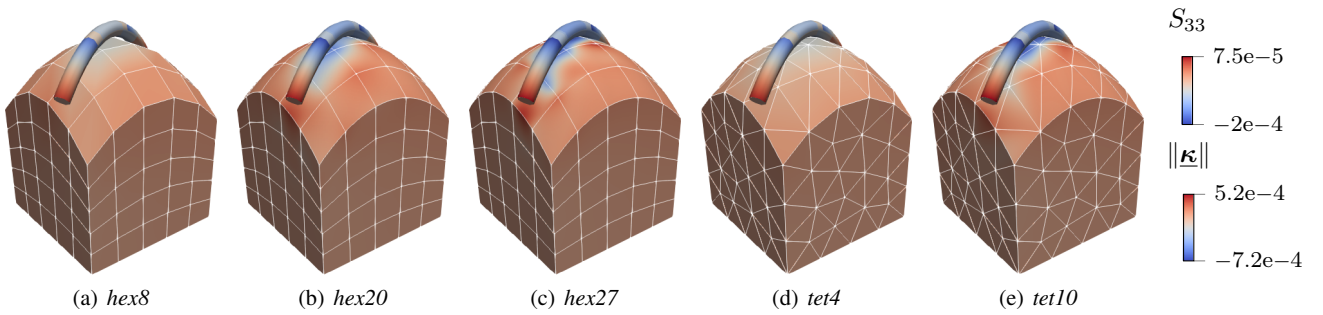


Fig. 14 Constant stress transfer – results for curved beams and various solid finite element discretizations. The coupling is modeled with the BTSS-FULL-CONS coupling variant. The second Piola-Kirchhoff stress S_{33} is shown in the solid and the curvature κ at the middle of each beam element. Note that the two beams Ω_{B1} and Ω_{B2} occupy the same spatial domain in the undeformed reference configuration.

introduced to further compare the three surface coupling types discussed in Sections 2.5 and 4.3. The solid half-pipe with length $l = 1$ m has an outer radius $r_a = 1$ m and an inner radius $r_i = 0.8$ m. The pipe is modeled using a compressible Neo-Hookean material law ($E_S = 1$ N/m², $\nu_S = 0$). The solid is coupled to a helix-shaped beam with a radius $r_b = 1.05$ m and a pitch of 2 m. The beam has a cross-section radius $R = 0.1$ m, Young's modulus $E_B = 50$ N/m² and Poisson's ratio $\nu_B = 0$. With the chosen geometric dimensions, the beam centerline does not exactly lie on the outer surface of the solid half-pipe, but is offset by a normal distance of 0.05 m. On one side of the half-pipe, a concentrated force $\underline{F} = 0.0004$ N \underline{e}_3 is applied to the tip of the beam. On the other side, the solid is fixed in all spatial directions.

Coupling between the beam and the solid is realized with the three BTSS-FULL coupling variants ($\epsilon_r = 10$ N/m², $\epsilon_\theta = 1$ Nm/m). First-order Lagrange polynomials are employed to discretize both the positional and the rotational Lagrange multipliers. The left part of Figure 16 illustrates the finite element discretization of the 1D-2D model. The pipe is modeled with $2 \times 12 \times 4$ finite elements in radial, tangential and \underline{e}_2 direction, respectively. Eight-noded solid shell elements are employed, cf. [6, 62]. The beam is discretized using 10 Simo–Reissner beam finite elements. In the

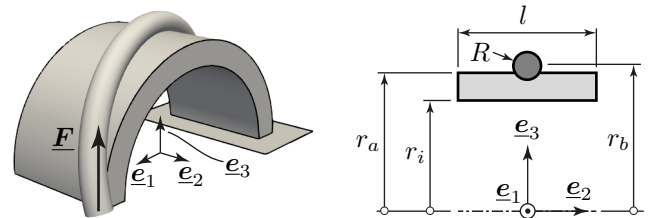


Fig. 15 Half-pipe with helix-shaped beam – problem setup. The left figure shows a 3D view of the problem and the right figure shows a cut through the $\underline{e}_2 - \underline{e}_3$.

present example, the beam cross-sections penetrate the solid coupling surface. Therefore, it is also possible to discretize this example with a full 3D finite element mesh, where the beam itself is also modeled using 3D finite elements, cf. the right part of Figure 16. The full 3D model is discretized with 50,480 second-order tetrahedra (*tet10*) elements. Consequently, the full 3D model consists of 226,383 degrees of freedom. The discretization of the full 3D model has been chosen such that mesh convergence is guaranteed and it can be used as a reference solution to assess the quality of the results obtained with the three BTSS-FULL variants.

Figure 17 visualizes the deformed configurations for the unloaded ($\underline{F} = \underline{0}$) structure. Since no pre-stressing or pre-

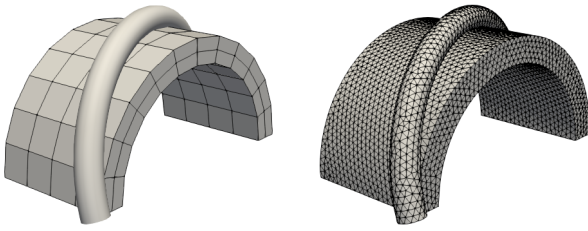


Fig. 16 Half-pipe with helix-shaped beam – finite element discretization of the beam-to-solid mesh (left) and full 3D mesh (right).

scribed initial deformations are applied to the structure, the analytical displacement field for the unloaded structure vanishes. The BTSS-FULL-REF variant exhibits non-vanishing displacements, cf. Figure 17(c). This is because the coupling constraints in the reference configuration are only fulfilled by the BTSS-FULL-REF variant (21) if the beam centerline lies exactly on the solid surface, which is not the case in this example. The coupling conditions thus force the beam centerline to lie on the solid surface. This in turn leads to an artificial pre-stressing of the system as both the beam and the solid are deformed in order to fulfill the coupling constraints in the load-free reference configuration. All other BTSS-FULL coupling variants and the full 3D solution exhibit vanishing displacements up to machine precision as expected. A quantitative comparison of the variants is given in Table 1. As discussed above, only the BTSS-FULL-REF variant has a non-zero internal elastic energy I_{int} (including the penalty coupling potential) and beam tip displacement \underline{u}_B for the load-free state. Figure 18 visualizes the deformed configurations for the loaded structure. It can be seen that the BTSS-FULL-CONS variant closely resembles the full 3D reference solution. The two other variants, BTSS-FULL-REF and BTSS-FULL-DISP, exhibit a different solution than the full 3D model. Again, quantitative comparisons of the variants are given in Table 2. The results for the BTSS-FULL-REF and BTSS-FULL-DISP show a large discrepancy with respect to the reference solution. For the BTSS-FULL-REF variant, this can easily be explained since already the initial (load-free) configuration does not match the reference solution. For the BTSS-FULL-DISP variant, this discrepancy illustrates that the simplified coupling conditions are not able to accurately describe the coupling between the beam and the solid surface if the discretized beam centerline does not exactly lie within the discretized solid surface in the reference configuration. Furthermore, the balance of internal and external moments around the origin shows that the conservation of angular momentum is not fulfilled by the BTSS-FULL-DISP variant. Finally, the internal elastic energy and the beam tip displacement obtained with the BTSS-FULL-CONS variant are very close to the reference solution, which is a remarkable feature considering the much simpler spatial discretization of the mixed-dimensional problem.

Summing up, after the first two examples we can state that both presented simplifications of the BTSS-FULL conditions, BTSS-FULL-REF and BTSS-FULL-DISP, are not suitable for general purpose BTSS coupling problems. Only the BTSS-FULL-CONS variant with a consistent handling of the surface normal vector, and its derivatives, passes the constant stress transfer tests and gives accurate results for more general loading conditions. Therefore, only this consistent variant will be used in the remainder of this contribution to model the positional coupling between beam and solid surface.

5.3 Supported plate

In this example the importance of coupling both positions *and* rotations within the BTSS coupling scheme is demonstrated. This is achieved by comparing the BTSS-FULL-CONS (including rotational coupling) and BTSS-POS-CONS (without rotational coupling) coupling schemes to each other. The problem consists of a plate and a straight beam serving as a strut, cf. Figure 19. The plate is loaded with a surface load $\underline{f} = 0.0002 \text{ N/m}^2 \underline{e}_3$ at the bottom surface. The dimensions of the plate are $3 \text{ m} \times 1 \text{ m} \times 0.1 \text{ m}$ and it is modeled using a compressible Neo-Hookean material law ($E_S = 1 \text{ N/m}^2$, $\nu_S = 0$). On the opposite face of the surface load, the plate is reinforced by a straight beam with circular cross-section ($R = 0.075 \text{ m}$, $E_B = 100 \text{ N/m}^2$ and $\nu_B = 0$). The beam centerline is parallel to the \underline{e}_1 axis and offset from the solid surface by a distance of R in surface normal direction, i.e., the beam cross-section exactly touches the solid surface. In \underline{e}_2 direction, the beam centerline is offset by a distance of 0.35 m with respect to the middle of the plate. At the right end, both solid and beam are fully clamped. Apart from that, no displacement boundary conditions are applied to the system.

A full 3D reference solution is computed, where the plate as well as the beam are fully resolved with 3D solid finite elements. In this reference solution, the connection between the beam and the plate, i.e., the weld line, has to be modeled. Figure 20 shows the fully resolved connection (weld line) between the beam and the plate which has a total width of $2R$. The weld line between beam and solid is assumed to be made up of the solid material. The full model is discretized with first-order hexahedral (*hex8*) elements, thus resulting in roughly 125,000 elements and 450,000 degrees of freedom to obtain mesh convergence.

In the 1D-2D BTSS coupling problem, the coupling between the beam and the solid surface is realized with first-order Lagrange polynomials as shape functions for the positional and the rotational Lagrange multipliers ($\epsilon_r = 100 \text{ N/m}^2$, $\epsilon_\theta = 0.1 \text{ Nm/m}$). The plate is modeled with $30 \times 10 \times 1$ eight-noded solid shell elements, cf. [6, 62]. The beam is discretized using 10 Simo–Reissner beam finite elements.

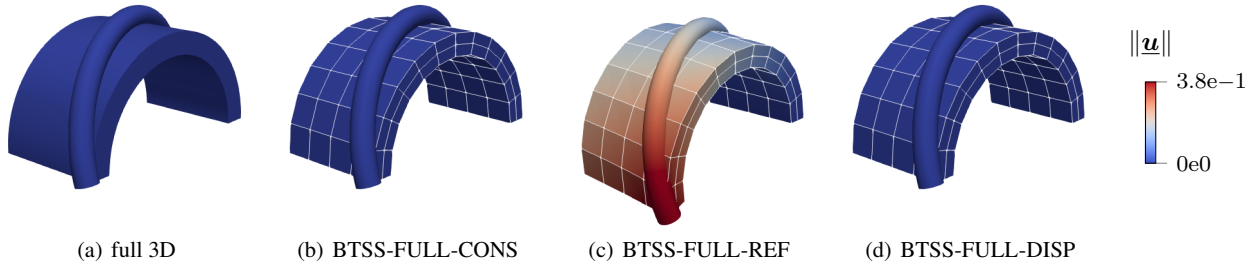


Fig. 17 Half-pipe with helix-shaped beam – deformed configurations for the unloaded problem ($\underline{F} = \underline{0}$). The results for the various coupling schemes are shown and the contour plots visualize the displacement magnitude.

Table 1 Half-pipe with helix-shaped beam – numerical results for the unloaded problem ($\underline{F} = \underline{0}$). The total internal elastic energy (including penalty coupling energy) Π_{int} and the beam tip displacement \underline{u}_B are stated.

coupling type	Π_{int} in $\text{J} \cdot 10^{-4}$	\underline{u}_B in m
full 3D	0.00000	[0.0, 0.0, 0.0]
BTSS-FULL-CONS	0.00000	[0.0, 0.0, 0.0]
BTSS-FULL-REF	3.37499	[0.24411, -0.37493, -0.03631]
BTSS-FULL-DISP	0.00000	[0.0, 0.0, 0.0]

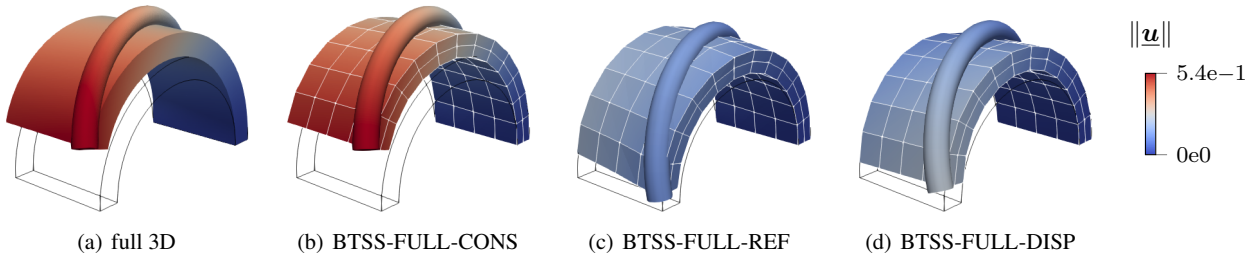


Fig. 18 Half-pipe with helix-shaped beam – deformed configurations for the loaded problem. The results for the various coupling schemes are shown and the contour plots visualize the displacement magnitude.

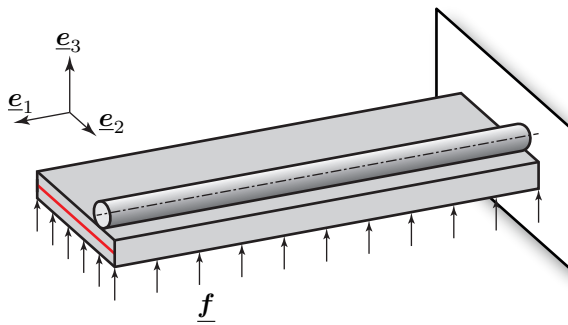


Fig. 19 Supported plate – problem setup. The red line indicates the material line for which the results are plotted in Figure 22.

The total number of degrees of freedom for the BTSS coupling problem is only 2,175.

Figure 21 visualizes the deformed configurations for the various models. The full 3D reference solution as well as the 1D-2D BTSS-FULL-CONS solution including rotational coupling behave very similarly, i.e., the plate is bent upwards and the strut stiffens the plate, cf. Figures 21(a) and 21(b).

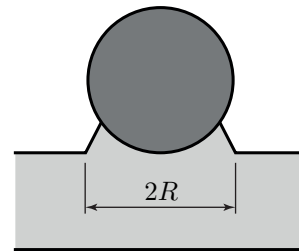


Fig. 20 Supported plate – modeled weld line between the beam and the plate in the full 3D reference solution.

The BTSS-POS-CONS variant without rotational coupling, however, exhibits much larger deformations. In that case, the rotational movement of the plate is not coupled to the rotations of the supporting beam, i.e., the torsional stiffness of the beam is not directly coupled to the solid plate, thus resulting in an overall softer structural behavior, cf. Figure 21(c). This clearly underlines the importance of including rotational coupling for BTSS coupling problems to fully capture all relevant stiffening effects. A more detailed comparison of the variants is given in Figure 22, where the displacements

Table 2 Half-pipe with helix-shaped beam – numerical results for the total internal elastic energy (including penalty coupling energy) Π_{int} and the beam tip displacement \underline{u} are stated as well as their relative error. Furthermore, the scaled sum of internal and external moments is stated.

coupling type	Π_{int} in $\text{J} \cdot 10^{-4}$	$\frac{\ \Pi_{\text{int}} - \Pi_{\text{int,full3D}}\ }{\ \Pi_{\text{int,full3D}}\ }$	\underline{u} in m	$\frac{\ \underline{u} - \underline{u}_{\text{full3D}}\ }{\ \underline{u}_{\text{full3D}}\ }$	$\frac{\ \Sigma(\underline{M}_{\text{int}} + \underline{M}_{\text{ext}})\ }{\ \underline{F}\ l}$
full 3D	1.14109	–	[-0.08411, 0.55495, -0.00476]	–	0.0000
BTSS-FULL-CONS	1.12581	1.3392%	[-0.08077, 0.54627, -0.00883]	1.8088%	0.0000
BTSS-FULL-REF	4.39811	285.4301%	[0.05225, 0.10224, -0.02442]	84.3041%	0.0000
BTSS-FULL-DISP	4.74429	58.4232%	[-0.03799, 0.22497, 0.05944]	60.4513%	126.5426

along the curve indicated in Figure 19 are visualized. Now it also becomes clear quantitatively that the displacement results obtained with the BTSS-POS-CONS variant without rotational coupling are unphysical due to the underestimated overall stiffness of the structure. Furthermore, the full 3D model and the BTSS-FULL-CONS model exhibit a very good agreement of the resulting displacement curves. Considering that the latter variant reduces the number of degrees of freedom by a factor of about 200, this is a remarkable result and showcases the efficiency of the BTSS-FULL-CONS coupling method for reinforced plate applications.

5.4 Towards biomedical applications

The last example is designed to give an outlook towards real-life applications and the suitability of the proposed BTSS-FULL approach for more complex coupling scenarios. Specifically, we want to analyze the applicability of our approach in the context of vascular angioplasty. To this end, we set up a variant of the well-known fluid-structure interaction (FSI) benchmark problem of a pressure wave traveling through an elastic tube, that was originally proposed in [17] to validate the suitability of FSI algorithms for blood flow simulations. In addition to the original problem, we will use our BTSS-FULL coupling approach to capture the effect of a diamond-shaped stent structure on the behavior of the overall system. In particular, we expect to capture the large change in compliance between the stented and unstented regions of the pipe, thus leading to stress peaks in these transitional regions as well as an altered fluid flow. Such effects have been linked to the occurrence of in-stent restenosis and are of high interest when analyzing the suitability of endovascular devices and their effect on the patient [11, 25, 27].

As in the original benchmark problem, a constant pulse p_{in} is applied for $3 \cdot 10^{-3}$ s at the fluid inlet. Besides the pulse, zero traction conditions are applied to the fluid inflow as well as outflow boundary on the left and right end of the pipe, respectively, while both ends of the pipe are assumed to be clamped. In addition to the BTSS-FULL problem introduced in Section 2, this example contains a fluid, modeled as Newtonian with a constant dynamic viscosity η_F and a density ρ_F , using the incompressible Navier-Stokes equations. Figure 23(a) illustrates the problem setup. The fluid is

Table 3 Table containing the parameters for the stented elastic pipe problem.

Geometry	r_i	0.0125 m
	r_a	0.01375 m
	r_s	0.01246 m
	l_1	0.15 m
	l_2	0.06 m
Beam	E_B	$9 \cdot 10^8 \text{ N/m}^2$
	ρ_B	7800 kg/m^3
	ν_B	0.3
	R	0.0004 m
Solid	E_S	$3 \cdot 10^5 \text{ N/m}^2$
	ρ_S	1200 kg/m^3
	ν_S	0.3
Fluid	p_{in}	500 N/m^2
	ρ_F	1000 kg/m^3
	η_F	0.003 kg/(ms)

coupled to the solid via classical surface-coupled FSI [26] in a partitioned manner aided by a matrix-free Newton Krylov method [31] to accelerate convergence. Classical no-slip conditions are enforced on the FSI boundary. The beam centerline geometry depicted in Figure 23(b) is wrapped around a cylinder with a radius of $r_s = r_i - R$ to create the used diamond-shaped stent geometry such that the stent perfectly fits into the pipe structure up to an offset the size of the beam radius. Since FSI problems are necessarily transient, the BTSS-FULL problem is enhanced by a Generalized- α Lie group time integration method for all structural degrees of freedom [7, 8]. Here, the parameters are chosen to obtain a fully implicit scheme, and a time step size $\Delta t = 10^{-4}$ s is used. To the fluid field, a classical second-order accurate Generalized- α time integration scheme, with the same time step size as for the structure field, is applied [21]. The mortar-type BTSS-FULL-CONS method is used with linear shape functions for the Lagrange multiplier fields and the penalty parameters $\epsilon_r = 10^9 \text{ N/m}^2$ and $\epsilon_\theta = 10^{-1} \text{ Nm/m}$. To discretize the problem, 264 Reissner beam elements, 2,880 solid shell elements and 22,800 PSPG/SUPG stabilized Q1-Q1 fluid elements with an additional div-grad stabilization term [50] are employed. All dimensions and material parameters of the problem setup are summarized in Table 5.4.

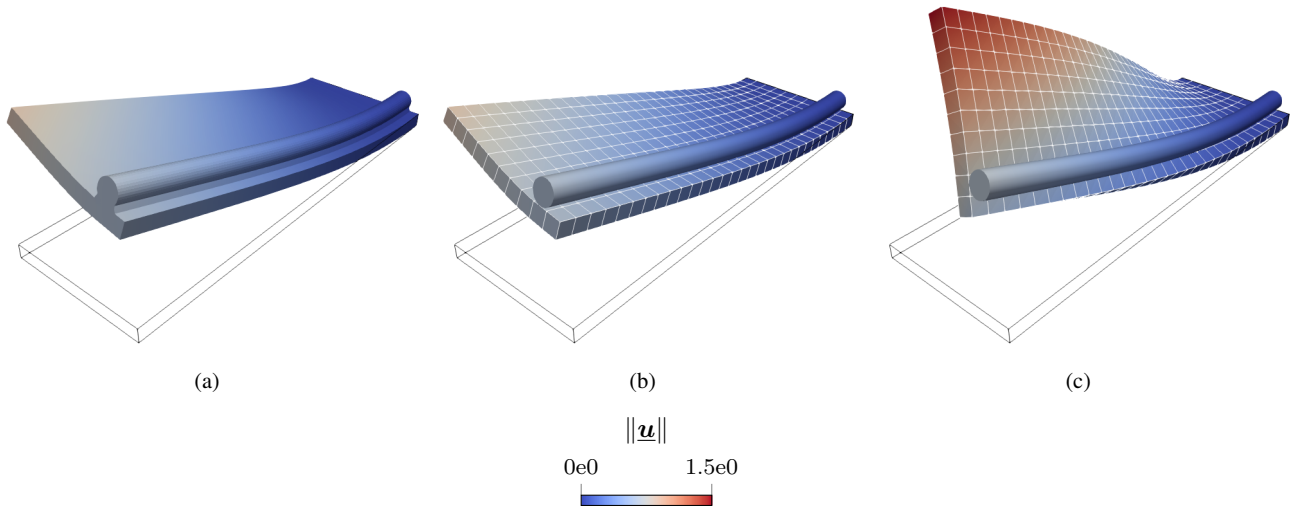


Fig. 21 Supported plate – deformed configurations for various modeling techniques. (a) Full 3D model, (b) BTSS-FULL-CONS (with rotational coupling) and (c) BTSS-POS-CONS (without rotational coupling). The contour plots visualize the displacement magnitude.

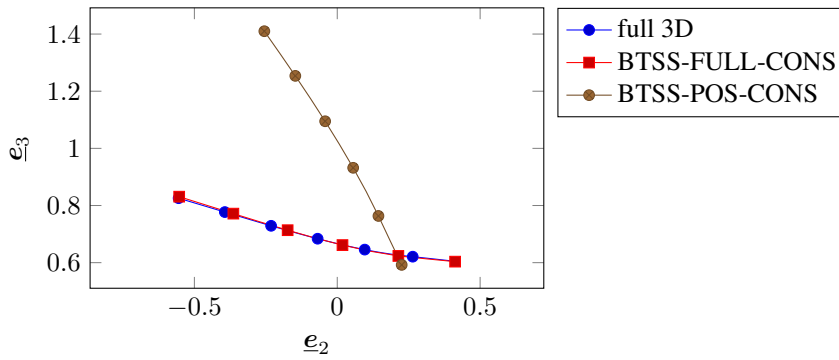


Fig. 22 Supported plate – deformed configurations of the material line indicated in Figure 19 for various modeling techniques.

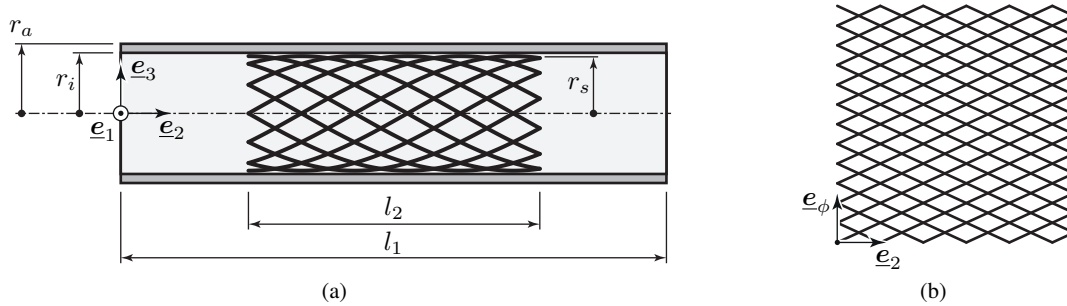


Fig. 23 Towards biomedical applications – problem setup. (a) Geometric configuration of the stent and artery, and (b) unwrapped stent geometry.

Figures 24(a) to 24(d) depict the structural displacement scaled with a factor of 15 and the fluid pressure after 0.01 s, 0.016 s, 0.024 s and 0.030 s. It is evident, that the wall displacement caused by the pressure wave in the stiffer stented region in Figure 24 is smaller than in the unstented region. This, in turn, affects the fluid since a constant flow throughput requires increased velocities within the stented region compared to the more compliant unstented region. Figure 25 illustrates the fluid velocity v_2 in channel direction along the

pipe’s centerline. The fluid velocity plot demonstrates the previously mentioned phenomenon as the maximum fluid velocity increases slightly and the wave broadens while traveling through the stented region. This effect on the fluid flow is still visible even after the pressure wave leaves the stented region.

While the change of compliance in the artery, and thus also its effect on the fluid flow, could also be modeled by a simpler homogenized approach, the proposed approach

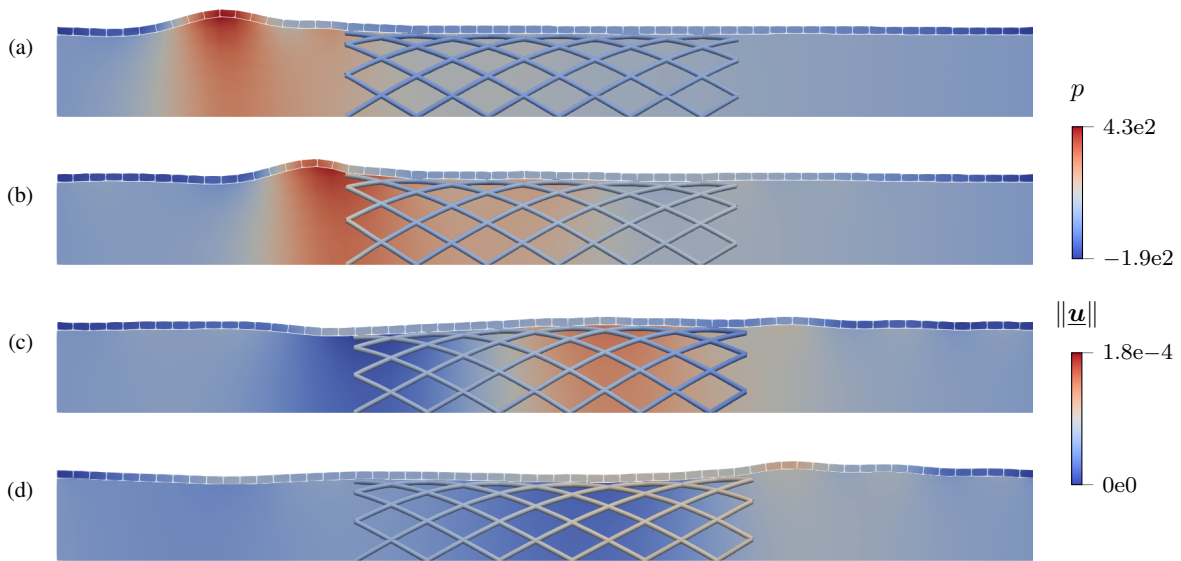


Fig. 24 Towards biomedical applications – deformed configuration of the stented elastic pipe problem at various simulation times. The snapshots are taken at (a) $t = 0.01$ s, (b) $t = 0.016$ s, (c) $t = 0.024$ s and (d) $t = 0.030$ s respectively. The norm of the displacements is shown in the solid and the pressure is shown in the fluid. The displacements are scaled with a factor of 15.

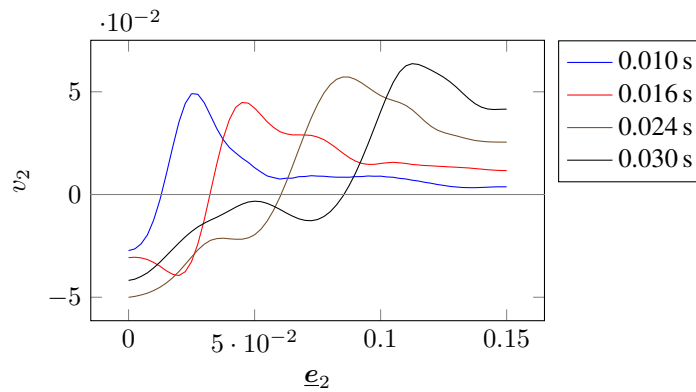


Fig. 25 Plots of the fluid velocity v_2 in channel direction along the pipe's centerline.

allows to quantify the forces interchanged on the coupling interface. Figures 26(a) and 26(d) illustrate the coupling interactions, i.e., the line loads exerted on the beam system by the surface. In general, it can be observed that the interaction is highest at the ends of the stent, i.e., at the transition between a compliant and a very stiff region. This is particularly notable in Figure 26(b), where the pressure wave is right at the transition between the unstented and stented region. Furthermore, dividing the 1D coupling loads by the beam diameter results in an approximation of the interaction stresses between the beam and the artery. The maximum absolute values of normal and shear stresses can be estimated for this example as $1.8179 \cdot 10^3$ N/m² and $1.28899 \cdot 10^3$ N/m² (not visualized in the figures), respectively.

The demonstrated example certainly represents a simplified model. In particular, the use of beam-to-solid surface coupling, as presented here, instead of frictional beam-to-

solid contact, prevents the observation of some real-life phenomena such as stent migration. Nevertheless, because of growth and remodeling of the artery and successive protrusion of the stent struts, coupling, i.e., mesh tying, is a valid assumption in many patient-specific cases. A further interesting novel computational method to incorporate was recently reported in [19]. It enables capturing the effect of the stent struts on the fluid flow, which is linked to altered wall shear stresses that may lead to in-stent restenosis [22, 36]. In any case, the presented simulation results serve as a proof of concept to show that the proposed BTSS-FULL coupling approach can generally be used for geometrically complex beam systems such as stent geometries. The ability to capture important phenomena, such as changes in compliance and its effect on the blood flow as well as the distribution of the interaction forces, which may provide insight into the long-term success of vascular angioplasty, has been demonstrated.

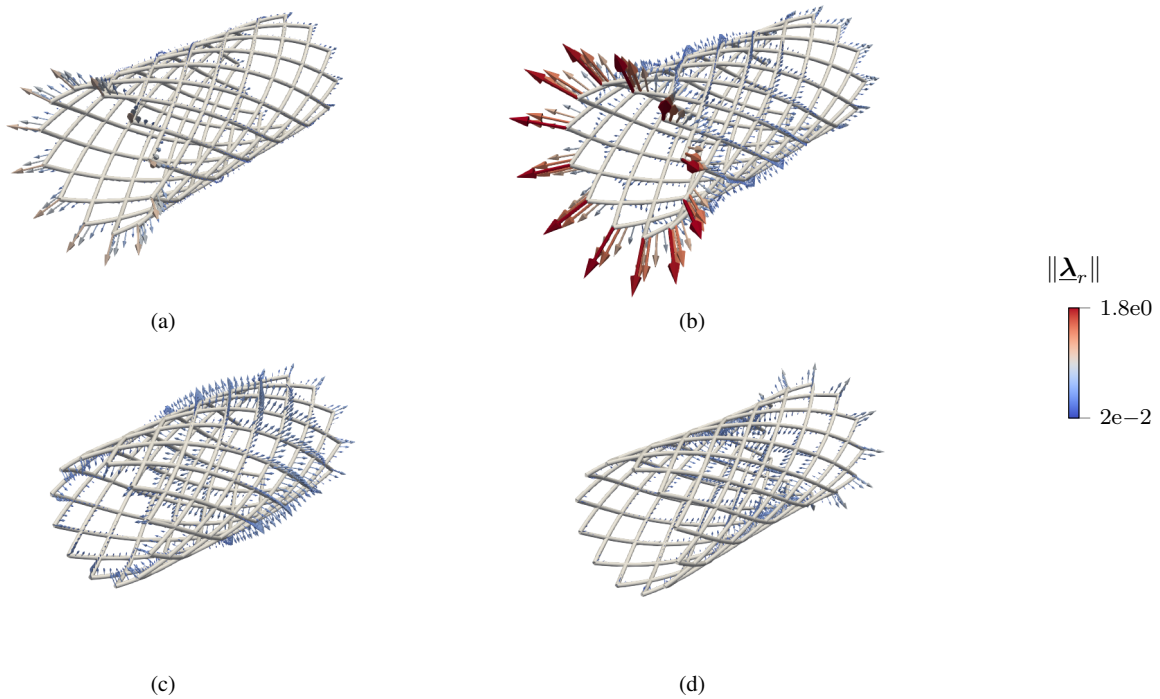


Fig. 26 Negative coupling line loads for beam-to-solid surface coupling at various simulation times – the snapshots are taken at (a) $t = 0.01$ s, (b) $t = 0.016$ s, (c) $t = 0.024$ s and (d) $t = 0.030$ s respectively. Only the positional Lagrange multiplier field is shown and five values are visualized along each beam element. The displacements are scaled with a factor of 15.

6 Conclusion

In this work, we have proposed a 1D-2D mixed-dimensional coupling method to consistently couple 1D Cosserat beams to 2D surfaces of 3D Boltzmann continua (solid). Therein, the six coupling constraints act along the beam centerline, i.e., three positional constraints and three rotational constraints. Three different variants of the positional coupling constraints have been investigated. One of them, the *consistent* variant, requires the expensive evaluation of the current surface normal field. The other two variants are commonly used in surface-to-surface mesh tying problems. Numerical examples have shown that only the consistent positional coupling constraints, i.e., with inclusion of the surface normal vector, lead to physically correct results and fulfill basic mechanical consistency properties, such as conservation of angular momentum. Existing coupling methods for the rotational degrees of freedom are extended by constructing a suitable surface triad field on the 2D surface of the 3D Boltzmann continuum. The Lagrange multiplier method is used to enforce the positional and rotational coupling constraints. The coupling equations are discretized using a mortar-type approach and the resulting discrete constraint equations are regularized via a weighted penalty approach. Furthermore, the numerical examples illustrate the importance of combining both positional *and* rotational coupling via a practically motivated example. Finally, a multi-physics simulation, in-

spired by models of stented arteries, has demonstrated the method's suitability for complex beam geometries and its ability to capture global effects on the solid as well as the fluid field.

Future work will focus on the extension of the presented beam-to-surface coupling approach to beam-to-surface contact and finite sliding problems, i.e., replacing the coupling constants with unilateral and frictional contact constraints.

Acknowledgements Sketches in this work have been created using the Adobe Illustrator plug-in LaTeX2AI (<https://github.com/isteinbrecher/LaTeX2AI>).

References

1. Argyris, J.: An excursion into large rotations. *Computer Methods in Applied Mechanics and Engineering* **32**(1), 85–155 (1982)
2. BACI: A Comprehensive Multi-Physics Simulation Framework. <https://baci.pages.gitlab.lrz.de/website> (2021)
3. Ben Belgacem, F.: The mortar finite element method with Lagrange multipliers. *Numerische Mathematik* **84**(2), 173–197 (1999)
4. Betsch, P., Menzel, A., Stein, E.: On the parametrization of finite rotations in computational mechanics: A classification of concepts with application to smooth

- shells. *Computer Methods in Applied Mechanics and Engineering* **155**(3), 273–305 (1998)
5. Betsch, P., Steinmann, P.: Frame-indifferent beam finite elements based upon the geometrically exact beam theory. *International Journal for Numerical Methods in Engineering* **54**(12), 1775–1788 (2002)
 6. Bischoff, M., Ramm, E.: Shear deformable shell elements for large strains and rotations. *International Journal for Numerical Methods in Engineering* **40**(23), 4427–4449 (1997)
 7. Brüls, O., Cardona, A.: On the use of Lie group time integrators in multibody dynamics. *Journal of Computational and Nonlinear Dynamics* **5**(3) (2010)
 8. Brüls, O., Cardona, A., Arnold, M.: Lie group generalized- α time integration of constrained flexible multibody systems. *Mechanism and Machine Theory* **48**, 121–137 (2012)
 9. Cardona, A., Geradin, M.: A beam finite element nonlinear theory with finite rotations. *International Journal for Numerical Methods in Engineering* **26**(11), 2403–2438 (1988)
 10. Chang, T.Y., Taniguchi, H., Chen, W.F.: Nonlinear finite element analysis of reinforced concrete panels. *Journal of Structural Engineering* **113**(1), 122–140 (1987)
 11. Colombo, M., He, Y., Corti, A., Gallo, D., Ninno, F., Casarin, S., Rozowsky, J., Migliavacca, F., Berceci, S., Chiastra, C.: In-stent restenosis progression in human superficial femoral arteries: Dynamics of lumen remodeling and impact of local hemodynamics. *Annals of Biomedical Engineering* **49**, 2349–2364 (2021)
 12. Crisfield, M.A., Jelenić, G.: Objectivity of strain measures in the geometrically exact three-dimensional beam theory and its finite-element implementation. *Proceedings of the Royal Society of London A* **455**(1983), 1125–1147 (1999)
 13. Dohrmann, C.R., Key, S.W., Heinstein, M.W.: Methods for connecting dissimilar three-dimensional finite element meshes. *International Journal for Numerical Methods in Engineering* **47**(5), 1057–1080 (2000)
 14. Durville, D.: Finite element simulation of textile materials at mesoscopic scale. In: *Finite element modelling of textiles and textile composites*. Saint-Petersbourg, Russian Federation (2007)
 15. Elwi, A.E., Hrudey, T.M.: Finite element model for curved embedded reinforcement. *Journal of Engineering Mechanics* **115**(4), 740–754 (1989)
 16. Farah, P., Popp, A., Wall, W.A.: Segment-based vs. element-based integration for mortar methods in computational contact mechanics. *Computational Mechanics* **55**(1), 209–228 (2015)
 17. Gerbeau, J.F., Vidrascu, M.: A quasi-Newton algorithm based on a reduced model for fluid-structure interaction problems in blood flows. *ESAIM: Mathematical Modelling and Numerical Analysis* **37**(4), 631–647 (2003)
 18. Gomes, H.M., Awruch, A.M.: Some aspects on three-dimensional numerical modelling of reinforced concrete structures using the finite element method. *Advances in Engineering Software* **32**(4), 257–277 (2001)
 19. Hagemeyer, N., Mayr, M., Steinbrecher, I., Popp, A.: One-way coupled fluid-beam interaction: Capturing the effect of embedded slender bodies on global fluid flow and vice versa. *Advanced Modeling and Simulation in Engineering Sciences* **9**(1), 9 (2022)
 20. Ibrahimbegović, A., Frey, F., Kožar, I.: Computational aspects of vector-like parametrization of three-dimensional finite rotations. *International Journal for Numerical Methods in Engineering* **38**(21), 3653–3673 (1995)
 21. Jansen, K., Whiting, C., Hulbert, G.: Generalized- α method for integrating the filtered Navier-Stokes equations with a stabilized finite element method. *Computer Methods in Applied Mechanics and Engineering* **190**, 305–319 (2000)
 22. Johari, N., Hamady, M., Xu, X.: A computational study of the effect of stent design on local hemodynamic factors at the carotid artery bifurcation. *Artery Research* **26**, 161 – 169 (2020)
 23. Kerfriden, P., Claus, S., Mihai, I.: A mixed-dimensional CutFEM methodology for the simulation of fibre-reinforced composites. *Advanced Modeling and Simulation in Engineering Sciences* **7**(1), 18 (2020)
 24. Khristenko, U., Schuß, S., Krüger, M., Schmidt, F., Wohlmuth, B., Hesch, C.: Multidimensional coupling: A variationally consistent approach to fiber-reinforced materials. *Computer Methods in Applied Mechanics and Engineering* **382**, 113869 (2021)
 25. Kim, Y.G., Oh, I.Y., Kwon, Y.W., Han, J.K., Yang, H.M., Park, K.W., Lee, H.Y., Kang, H.J., Koo, B.K., Kim, H.S.: Mechanism of edge restenosis after drug-eluting stent implantation. *Circulation Journal* **77**, 2928–2935 (2013)
 26. Klöppel, T., Popp, A., Küttler, U., Wall, W.A.: Fluid-structure interaction for non-conforming interfaces based on a dual mortar formulation. *Computer Methods in Applied Mechanics and Engineering* **200**(45), 3111–3126 (2011)
 27. Kohler, T.R., Jawień, A.: Flow affects development of intimal hyperplasia after arterial injury in rats. *Arteriosclerosis and thrombosis: A journal of vascular biology* **12**, 963–71 (1992)
 28. Konyukhov, A., Schweizerhof, K.: On the solvability of closest point projection procedures in contact analysis: Analysis and solution strategy for surfaces of arbitrary geometry. *Computer Methods in Applied Mechanics and Engineering* **197**(33), 3045–3056 (2008)

29. Konyukhov, A., Schweizerhof, K.: On some aspects for contact with rigid surfaces: Surface-to-rigid surface and curves-to-rigid surface algorithms. *Computer Methods in Applied Mechanics and Engineering* **283**, 74–105 (2015)
30. Korelc, J., Wriggers, P.: *Automation of finite element methods*. Springer International Publishing (2016)
31. Küttler, U., Wall, W.A.: Fixed-point fluid-structure interaction solvers with dynamic relaxation. *Computational Mechanics* **43**(1), 61–72 (2008)
32. Meier, C., Grill, M.J., Wall, W.A.: Generalized section-section interaction potentials in the geometrically exact beam theory (2021). Preprint, <https://arxiv.org/abs/2105.10032>
33. Meier, C., Popp, A., Wall, W.A.: An objective 3D large deformation finite element formulation for geometrically exact curved Kirchhoff rods. *Computer Methods in Applied Mechanics and Engineering* **278**, 445–478 (2014)
34. Meier, C., Popp, A., Wall, W.A.: A finite element approach for the line-to-line contact interaction of thin beams with arbitrary orientation. *Computer Methods in Applied Mechanics and Engineering* **308**, 377–413 (2016)
35. Meier, C., Popp, A., Wall, W.A.: Geometrically exact finite element formulations for slender beams: Kirchhoff–Love theory versus Simo–Reissner theory. *Archives of Computational Methods in Engineering* **26**(1), 163–243 (2019)
36. Pant, S., Bressloff, N.W., Forrester, A.I.J., Curzen, N.: The influence of strut-connectors in stented vessels: A comparison of pulsatile flow through five coronary stents. *Annals of Biomedical Engineering* **38**, 1893–1907 (2010)
37. Park, K.C., Felippa, C.A., Rebel, G.: A simple algorithm for localized construction of non-matching structural interfaces. *Int. J. Numer. Meth. Engng.* **53**(9), 2117–2142 (2002)
38. Phillips, D.V., Zienkiewicz, O.C.: Finite element non-linear analysis of concrete structures. *Proceedings of the Institution of Civil Engineers* **61**(1), 59–88 (1976)
39. Podio-Guidugli, P.: Examples of concentrated contact interactions in simple bodies. *Journal of Elasticity* **75**(2), 167–186 (2005)
40. Podio-Guidugli, P., Favata, A.: *Elasticity for geotechnicians: A modern exposition of Kelvin, Boussinesq, Flamant, Cerruti, Melan, and Mindlin problems*, vol. 204. Springer, Cham (2014)
41. Popp, A., Gee, M.W., Wall, W.A.: A finite deformation mortar contact formulation using a primal–dual active set strategy. *International Journal for Numerical Methods in Engineering* **79**(11), 1354–1391 (2009)
42. Popp, A., Gitterle, M., Gee, M.W., Wall, W.A.: A dual mortar approach for 3D finite deformation contact with consistent linearization. *International Journal for Numerical Methods in Engineering* **83**(11), 1428–1465 (2010)
43. Puso, M.A.: A 3D mortar method for solid mechanics. *International Journal for Numerical Methods in Engineering* **59**(3), 315–336 (2004)
44. Puso, M.A., Laursen, T.A.: A mortar segment-to-segment contact method for large deformation solid mechanics. *Computer Methods in Applied Mechanics and Engineering* **193**(6), 601–629 (2004)
45. Puso, M.A., Laursen, T.A.: A mortar segment-to-segment frictional contact method for large deformations. *Computer Methods in Applied Mechanics and Engineering* **193**(45), 4891–4913 (2004)
46. Ranjbaran, A.: Mathematical formulation of embedded reinforcements in 3D brick elements. *Communications in Numerical Methods in Engineering* **12**(12), 897–903 (1996)
47. Reissner, E.: On one-dimensional finite-strain beam theory: The plane problem. *Zeitschrift für angewandte Mathematik und Physik ZAMP* **23**(5), 795–804 (1972)
48. Romero, I.: The interpolation of rotations and its application to finite element models of geometrically exact rods. *Computational Mechanics* **34**(2), 121–133 (2004)
49. The Sacado Project Website. <https://trilinos.github.io/sacado.html> (2021)
50. Schott, B., Rasthofer, U., Gravemeier, V., Wall, W.A.: A face-oriented stabilized Nitsche-type extended variational multiscale method for incompressible two-phase flow. *International Journal for Numerical Methods in Engineering* **104**(7), 721–748 (2015)
51. Simo, J.C., Vu-Quoc, L.: On the dynamics of flexible beams under large overall motions – The plane case: Part I. *Journal of Applied Mechanics* **53**(4), 849–854 (1986)
52. Simo, J.C., Vu-Quoc, L.: On the dynamics of flexible beams under large overall motions – The plane case: Part II. *Journal of Applied Mechanics* **53**(4), 855–863 (1986)
53. Sonnevile, V., Cardona, A., Brüls, O.: Geometrically exact beam finite element formulated on the special Euclidean group SE(3). *Computer Methods in Applied Mechanics and Engineering* **268**, 451–474 (2014)
54. Spurrier, R.A.: Comment on "Singularity-free extraction of a quaternion from a direction-cosine matrix". *Journal of Spacecraft and Rockets* **15**(4), 255–255 (1978)
55. Steinbrecher, I., Mayr, M., Grill, M.J., Kremheller, J., Meier, C., Popp, A.: A mortar-type finite element approach for embedding 1D beams into 3D solid volumes. *Computational Mechanics* **66**(6), 1377–1398 (2020)
56. Steinbrecher, I., Popp, A.: MeshPy – A general purpose 3D beam finite element input generator. <https://compsim.gitlab.io/codes/meshpy> (2021)

57. Steinbrecher, I., Popp, A., Meier, C.: Consistent coupling of positions and rotations for embedding 1D Cosserat beams into 3D solid volumes. *Computational Mechanics* **69**(3), 701–732 (2022)
58. Taylor, R.L., Simo, J.C., Zienkiewicz, O.C., Chan, A.C.H.: The patch test – A condition for assessing FEM convergence. *International Journal for Numerical Methods in Engineering* **22**(1), 39–62 (1986)
59. Thomson, W.: Note on the integration of the equations of equilibrium of an elastic solid. *The Cambridge and Dublin mathematical journal* **3**, 87–89 (1848)
60. The Trilinos Project Website. <https://trilinos.github.io> (2021)
61. Vetyukov, Y.: *Nonlinear mechanics of thin-walled structures: Asymptotics, direct approach and numerical analysis*. Foundations of Engineering Mechanics. Springer (2014)
62. Vu-Quoc, L., Tan, X.G.: Optimal solid shells for nonlinear analyses of multilayer composites. I. Statics. *Computer Methods in Applied Mechanics and Engineering* **192**(9), 975–1016 (2003)
63. Wohlmuth, B.I.: A mortar finite element method using dual spaces for the lagrange multiplier. *SIAM Journal on Numerical Analysis* **38**(3), 989–1012 (2000)
64. Yang, B., Laursen, T.A., Meng, X.: Two dimensional mortar contact methods for large deformation frictional sliding. *International Journal for Numerical Methods in Engineering* **62**(9), 1183–1225 (2005)